

Article

Comparative Study on the Corrosion Inhibitive Effect of 2-Mercaptobenzothiazole and Na₂HPO₄ on Industrial Conveying API 5L X42 Pipeline Steel

Ioannis A. Kartsonakis , Panagiota Stamatogianni, Evangelia K. Karaxi and Costas A. Charitidis * 

Research Unit of Advanced, Composite, Nano-Materials and Nanotechnology, School of Chemical Engineering, National Technical University of Athens, 9 Heron Polytechniou St., Zographos, GR-15773 Athens, Greece; ikartso@chemeng.ntua.gr (I.A.K.); giota_grock.n.metal@hotmail.com (P.S.); dcar@chemeng.ntua.gr (E.K.K.)

* Correspondence: charitidis@chemeng.ntua.gr; Tel.: +30-2107724046

Received: 1 December 2019; Accepted: 27 December 2019; Published: 31 December 2019



Abstract: Mild or low-carbon steel has an increasing utilization and is widely used for building construction, machinery parts, and pipelines, because it can be machined easily and has enhanced weldability as well as a low price. In any case, the corrosion resistance of mild steel under the conditions in industrial applications or in atmosphere is a thoughtful concern. This study inquires into the application of 2-mercaptobenzothiazole (MBT) and Na₂HPO₄ as corrosion inhibitors for the protection of API 5L X42 pipeline steel in 3.5 wt % NaCl as well as in water from the Athens city supply system. The electrochemical/morphological characterizations of the aforementioned mild steel proved that the corrosion protection mechanisms can be assigned to the protective layers created onto the metal surface because of the presence of the inhibitors, which prevent chloride's penetration. The synergistic effect of the MBT and Na₂HPO₄ corrosion inhibition behavior, in a molar ratio of 1:1, revealed that the additives performed effectively with corrosion inhibition efficiency above 90%.

Keywords: mild steel; EIS; SEM; Raman spectroscopy; pitting corrosion; synergistic effect

1. Introduction

One of the most widespread kinds of steel is low-carbon or mild steel, not only for structural purposes but also for several applications in industry. Therefore, its usage and operation range from machinery parts, building materials, and domestic appliances to cutting tools, conveying tubes, cables, and magnets. Due to its low concentration in carbon (up to 0.29 wt %), mild steel exhibits extreme durability, great affordability, and significant mechanical, thermal, and magnetic properties [1–3]. Due to mild steel's increasing utilization, there has been great concern for the susceptibility of such steels caused by environmental corrosive factors, such as the humidity, acidity, or salinity of the atmosphere [4–6]. Thus, lots of studies have been focusing on low-alloy (weathering) steel corrosion and how to encounter it in a functional way [7–9].

In general, metallic corrosion is associated with any chemical alteration of the metal that stems from interaction with its environment [10]. Although intense research studies have taken place over all these decades in order to face corrosion, it still remains in the foreground since it is a continuous and inevitable process [11]. The main classification of corrosion types emphasized in the literature is between uniform and localized corrosion [12]. Pitting corrosion is a type of localized corrosion in which the metal is corroded in depth via the formation of indistinguishable pits. In the case of water and usually oil-conveying pipes, the corrosion effect often triggers uniform surface degradation internally, in parallel with localized corrosion underneath and oxide film formation [13,14]. Taking into

account that pitting may cause the initiation of stress corrosion cracking [15], it is considered as the most detrimental corrosion effect. While uniform corrosion occurs during the subjection of mild steel in various environmental conditions [8,16], localized corrosion, such as pitting and scaling, takes place in the presence of heavy metal ions [17,18] or in locally high pH values [19]. Localized corrosion phenomena may thin locally the inner wall in a pipe, resulting in the creation of areas susceptible to cracking [20].

The protection of metallic materials from the corrosion effect could be achieved by intervening either in the alloy structure or in the alloy environment. The intervention in the alloy structure can be performed by changing the alloying ratio, by creating/applying metallic or organic coatings/films on the surface, by decreasing mechanical operation tensions, by the use of anodic or cathodic protection, and by adding corrosion inhibitors in the corroding solution [21]. In the literature, several studies indicate corrosion inhibition as an effective protection method [22,23]. A conventional classification of corrosion inhibitors is according to their inhibiting action. Therefore, there are adsorption inhibitors that undergo chemisorption in the metallic surface, film-forming inhibitors, which are divided into passivation inhibitors (oxidizing or non-oxidizing) and precipitation inhibitors (deposition of three-dimensional film). However, the most common discrimination is between anodic, cathodic, and mixed-type inhibitors, considering which half-reaction they suppress during corrosion phenomena. Most organic inhibitors are of mixed-type and act as chemisorptive inhibitors. Phosphates act as cathodic inhibitors, whereas benzoates and azelates represent non-oxidizing film-forming inhibitors [24].

Concerning inorganic inhibitors, ideally the central atom of the inhibitor tends to form a complex entering the metallic lattice, without the need of additional energy and with the necessary stability [25]. Refaey et al. compared the inhibition ability of phosphate, chromate, molybdate, and nitrite as potential inhibitors for mild steel, in 0.1 M NaCl near neutral solutions. They concluded that phosphate demonstrated higher inhibition efficiency compared to the other inhibitors. Furthermore, phosphate deposited a strongly adherent layer, consisting of γ -Fe₂O₃ and FePO₄·2H₂O, from the solution on the metal surface [26]. Regarding organic corrosion inhibitors, a perusal of the literature reveals a variety of organic compounds that have been suggested for encountering pitting corrosion on mild steel. An outstanding investigation was carried out by Marczewska-Boczkowska and Kosmulski using steel samples in aqueous solutions and indicating certain derivatives of azoles and thiazoles. They reported that imidazoles, benzothiazoles, and mercaptobenzothiazoles behaved as significantly efficient corrosion inhibitors against pitting. They claimed that these organic substances are capable of forming self-assembled monolayers, which improve inhibition and confer a protective layer of great stability, due to the spontaneous self-assembly process [27]. Moreover, Wang et al. synthesized and utilized an organic chemical compound, 4-salicylideneamino-3-phenyl-5-mercapto-1,2,4-triazole, as a corrosion inhibitor for mild steel, in electrolytic solution of 1 M HCl solution in several temperatures, which was based on the enhanced corrosion inhibition of the combined N and S elements in heterocyclic organic compounds [26]. They also pointed out that the presence of both elements functions more efficiently instead of the use of substances that contain only nitrogen or sulfur separately. This outcome was attributed to the combination of phenyl, mercapto, and azomethine reactive groups. Taking into account these claims, 2-mercaptobenzothiazole (MBT) was rendered as one of the most preferable mixed-type organic inhibitors for mild steel in aqueous solutions [28].

The self-assembling effect [29] and the chemisorption ability in conjunction with the aromatic nature of the inhibitor, which confers increased stability [25], lead to the need to investigate how to optimize inhibition by the use of MBT. Furthermore, its efficiency in near neutral aqueous solutions was taken into account. A common utilization of MBT was in coolant mixtures as a corrosion inhibitor for low-carbon steel pipes [30]. It exhibited improved inhibition efficiency when mixed with different organic inhibitors, denoting the advanced synergistic inhibition effect through smart combinations. Gunasekaran et al. evaluated the synergistic corrosion inhibition of several phosphonic acids substituting metal ions for azoles, provided that phosphorous inhibition ability could be exploited in chemically different systems [31]. A conventional use of phosphate anions in corrosion inhibitors is in

cooling systems that maintain cavitation problems and intense corrosion phenomena [32]. Calmon et al. patented certain mixtures against pitting and the galvanic corrosion of copper and iron surface, consisting of sodium phosphates (Na_2HPO_4) or polyphosphates ($\text{Na}_2\text{P}_4\text{O}_{13}$) synergistically with sodium mercaptobenzothiazole in aqueous solutions emphasizing the immediate connection between inhibition efficiency and inhibitor concentration [33].

The aim of this study is to investigate the susceptibility of mild steel to corrosion in industrial hot/cooling systems after its exposure in 3.5 wt % NaCl as well as in the water of the Athens city supply system. The main goal of the presented experiments is to identify which inhibitors perform best at restricting the aforementioned corrosion process. The importance of these experiments is directly linked to the current urgent need for industrial mild steel pipeline corrosion protection.

In this regard, the protection effectiveness of the complexes, oxides, or salts that are created on the mild steel surface, as well as the morphological conversions that occur on the surface of the metal alloy panels following exposure in the presence or absence of MBT and Na_2HPO_4 , were evaluated by three families of techniques: electrochemical, microscopy, and spectroscopy. The electrochemical characterization demonstrated that MBT and Na_2HPO_4 can be considered as corrosion inhibitors of mild steel as they reduced the corresponding anodic and/or cathodic corroding reactions. Moreover, the synergistic effect of the corrosion inhibition behavior of MBT and Na_2HPO_4 in a molar ratio 1:1 at several concentrations was studied. The analysis revealed that the admixtures performed effectively with inhibition efficiency above 90%. The presence of both aforementioned inhibitors into the corrosive environment exhibited the highest impedance modulus ($|Z|$) and polarization resistance (R_p) value as the exposure time elapsed.

Regarding the X-ray diffraction (XRD) measurements and scanning electron microscopy (SEM) characterization, it was disclosed that the exposure of mild steel to a corrosive environment in the presence or absence of inhibitors resulted in the creation of several oxide, hydroxide, and hydroxide–phosphate compounds on the steel surface. According to the aforementioned characterization techniques, the corrosion protection mechanisms of steel can be ascribed to the protective films created onto the metal surface because of the inhibitors' presence, which prevent chlorides' insertion. The performed experiments shed light on the corrosion mechanisms of mild steel in industrial hot/cooling systems.

2. Materials and Methods

2.1. Reagents and Solutions

All the compounds and reagents were of analytical reagent grade. Sodium phosphate dibasic dihydrate ($\text{Na}_2\text{HPO}_4 \cdot 2\text{H}_2\text{O}$, Sigma-Aldrich) and 2-mercaptobenzothiazole (MBT, Sigma-Aldrich) were used without further purification. Hot-rolled black (non-galvanized) mild steel panels were manufactured by TMK-ARTROM S.A. and accompanied with all certifications required (ASTM A568/A568M-09 [34]). Electrochemical measurements were performed on mild steel grade API 5L X42 conveying a pipeline with the following chemical composition (wt %): C: 0.15, Mn: 0.56, S: 0.002, P: 0.12, Si: 0.21, Ni: 0.07, Cr: 0.04, Mo: 0.01, Cu: 0.22, Al: 0.020, N: 0.009, V+Ti+Nb: 0.004, and Fe as remainder.

2.2. Preparation of Substrates

The mild steel panels were abraded with SiC paper up to 5 μm grain size (P4000) and then cleaned in agreement with ASTM D6386-99 (reapproved 2005) [35] prior to being used in the conducted experiments. This procedure is necessary because the exposed steel interacts with the environment to form several iron oxides such as $\alpha\text{-FeO(OH)}$, $\gamma\text{-FeO(OH)}$, $\beta\text{-FeO(OH)}$, and Fe_3O_4 [36]. According to the aforementioned standard, the cleaning procedure includes the degreasing of steel panels with their subjection in a mixture of acetone and ethanol (50:50) of purity 96% *v/v* for about 20 min, and then their exposure to NaOH solution of pH 11 for 5 min at 60 °C. Finally, the panels are rinsed with distilled

water and dried in a desiccator in order to avoid the formation of new corrosion products, as uncoated black mild steel is susceptible to corrosion by humidity, as analyzed above.

2.3. Characterization

Several imaging techniques providing information at macro- and microscopic scales were used in order to evaluate the surface morphology of the mild steel panels. The microscale information was collected with SEM imaging performance using a Hitachi Tabletop Microscope TM3030 Scanning Electron Microscopy equipped with an energy dispersive X-ray spectrophotometer (EDS) system (QUANTAX 70), and with an ultra-high resolution scanning electron microscopy (UHR-SEM) using NOVA NANOSEM 230 (FEI Company). The macroscale information with respect to optical details was acquired using a Samsung Galaxy A7 auto focus triple camera 24 MP + 5 MP + 8 MP. The chemical analysis was conducted via micro-Raman measurements using a Renishaw inVia spectrometer working in backscattering configuration and equipped with a near-infrared diode laser emitting at 532 and 785 nm. The spectra were recorded by focusing the laser beam on the sample surface and adjusting the light power so that 1 mW was provided for a spot of about 1 μm diameter. The compounds that are created on the subjected mild steel panels were studied via XRD measurements. The crystal structure was identified by powder X-ray diffraction using an X Bruker D8 Advance Twin Twin, employing Cu-K α radiation ($\lambda = 1.5418 \text{ \AA}$).

The electrochemical characterizations based on linear polarization resistance (LPR) and potentiodynamic polarization (PP) were conducted using a VersaSTAT 3 Potentiostat/Galvanostat/Frequency Response Analyzer instrument (Princeton Applied Research, AMETEK). Concerning the PP measurements, a three-electrode electrochemical cell was used, consisting of a saturated silver chloride electrode [Ag/AgCl, KCl_(sat)] as reference, a working electrode ($\approx 1.0 \text{ cm}^2$ of exposed area), and a platinum foil as counter electrode. The assessment of the polarization curves on the bare alloy was accomplished after different exposure intervals. Cathodic and anodic branches of polarization curves were recorded separately with the potential scan rate of 1 mVs^{-1} in the cathodic and in the anodic directions, starting from the open circuit potential (OCP, E_{OC} , corrosion potential), at room temperature. Regarding the LPR measurements, the scan rate was 0.1 mVs^{-1} and the potential range was $\pm 2.5 \text{ mV}$ versus OCP. The R_p (polarization resistance) is the definition of the ratio of the applied potential to the applied current ($\Delta E/\Delta I$). The slope of the potential versus current plot is used for the calculation of the R_p [37]. The R_p denotes the degree of the specimen susceptibility to be corroded [38,39]. The corrosion protection performance of the inhibitors was estimated via electrochemical impedance spectroscopy (EIS). The EIS measurements were conducted using the aforementioned potentiostat instrument with the arrangement of the three-electrode electrochemical cell, in a frequency range from 10 μHz to 1 MHz. All spectra were recorded at open circuit potential, applying a 10 mV sinusoidal perturbation (rms signal) at room temperature. During all measurements, the electrochemical cell was placed in a Faraday cage. The Z-view Software (Scribner Associates Incorporated, SAI) was used for the analysis of the obtained spectra utilizing the adequate equivalent electric circuits. Two different types of electrolytic solutions (300 mL) were used: (i) water from the supply system of Athens city (WSS: water of the Athens city supply system after a softening process, Table 1), and (ii) 3.5 wt % NaCl solution prepared in distilled water [ASTM G44-99 (2013)] [40].

Table 1. Ion composition of the water of the Athens city supply system after a softening process (WSS) estimated via atomic absorption spectroscopy (mg/L).

K	Ca	Mg	Fe	Mn	Zn
1.7733	0.346	0.09755	1.36	0.005	0.0052

Moreover, the corrosion phenomena on a metallic uncoated surface was further evaluated with respect to the influence of corrosion inhibitors. Consecutively, 6 mM electrolytic solutions of the

impending corrosion inhibitors were prepared for each compound as well as certain equimolecular 6 mM solutions of both Na_2HPO_4 and MBT for the investigation of their synergistic inhibition effect (Table 2). The sample *Steel-blank* is ascribed to mild steel panel prior to subsection in electrolytic solutions.

Table 2. Composition of the solutions for testing the effectiveness of the inhibitors onto mild steel. Reagents concentration 6 mM, reagents solubility in water (mg/100 g, 20 °C) 1.7×10^3 Na_2HPO_4 , 1.9×10^1 MBT.

Composition	pH	Sample
-	-	<i>Steel-blank</i>
WSS	7.41–7.52	<i>Steel-WSS-blank</i>
WSS + 0.849 g/L Na_2HPO_4	7.78–7.97	<i>Steel-WSS-Na_2HPO_4</i>
WSS + 1.014 g/L MBT	7.33–7.52	<i>Steel-WSS-MBT</i>
WSS + 0.849 g/L Na_2HPO_4 + 1.014 g/L MBT	7.38–7.82	<i>Steel-WSS-Na_2HPO_4-MBT</i>
NaCl 3.5 wt %	7.71–7.72	<i>Steel-NaCl-blank</i>
NaCl 3.5 wt % + 0.849 g/L Na_2HPO_4	7.78–7.97	<i>Steel-NaCl-Na_2HPO_4</i>
NaCl 3.5 wt % + 1.014 g/L MBT	7.33–7.52	<i>Steel-NaCl-MBT</i>
NaCl 3.5 wt % + 0.849 g/L Na_2HPO_4 + 1.014 g/L MBT	7.38–7.82	<i>Steel-NaCl-Na_2HPO_4-MBT</i>

The corrosion inhibition efficiency, $\eta(\%)$, was estimated by Equation (1):

$$\eta(\%) = \frac{R_{ct(\text{inhibitor})} - R_{ct(\text{bareMetal})}}{R_{(\text{inhibitor})}} \times 100 \quad (1)$$

where $R_{ct(\text{inhibitor})}$ and $R_{ct(\text{bareMetal})}$ represent the charge transfer resistances in the presence and in the absence of an inhibitor, respectively [41,42].

The synergistic parameter (S_i) was calculated from Equation (2) given by Aramaki and Hackerman [43]:

$$S_i = \frac{1 - \eta_{1+2}}{1 - \eta_{1+2}^*}, \quad (2)$$

where η_1 is the inhibition efficiency of the Na_2HPO_4 , η_2 is the inhibition efficiency of the MBT, and $\eta_{1+2} = (\eta_1 + \eta_2) - (\eta_1 \times \eta_2)$, η_{1+2}^* is the measured inhibition efficiency of the MBT in combination with Na_2HPO_4 .

3. Results and Discussion

3.1. Morphology Evaluation

The visual pictures of mild steel immersed in WSS for 96 h, in the presence of inhibitors or not, are demonstrated in Figure 1a–d. Onto the slightly rinsed corroded surface of Figure 1a, ferrous yellowish, orange, and brownish red species create a hardly homogenous layer, as expected from the literature for the mild steel surface in the absence of inhibitors (*Steel-WSS-blank*). Susceptible to a series of local corrosion phenomena as well as to the creation of local galvanic cells and pits, the final layer emerges in dependence with the local composition and physicochemical conditions of the system [44]. In depth, it is claimed that reddish hues stem from hematite ($\alpha\text{-Fe}_2\text{O}_3$) in a hexagonal crystal system, in which the face-sharing octahedral keeps the Fe centers at the shortest distance (0.29 nm), whereas the yellowish ones are caused by the edge- or/and corner-sharing octahedral of lepidocrocite [$\gamma\text{-FeO(OH)}$], maghemite ($\gamma\text{-Fe}_2\text{O}_3$), goethite [$\alpha\text{-FeO(OH)}$] and other compounds, with Fe center distances from 0.30 to 0.35 nm. In the presence of each inhibitor separately, the mild steel surface is either converted by the phosphate invasion into the crystal lattice, in case of phosphate solution in *Steel-WSS- Na_2HPO_4* (Figure 1b), or covered by the organic three-dimensional organic layer precipitated, in the case of MBT in *Steel-WSS-MBT* (Figure 1c). In mere phosphate solutions, the lack of reddish corrosion products and the development of a thinner and yellower final layer, as shown in Figure 1b (*Steel-WSS- Na_2HPO_4*)

and Figure 1f (*Steel–NaCl–Na₂HPO₄*), are characteristic of the corrosion process due to the hindrance of hematite formation, as detailed below. Since the earlier stages and according to the literature, the inner layer (2D layer) is expected to consist of gray and blackish magnetite (Fe₃O₄) and maybe wustite (FeO). Supplementary to the electrochemical and spectroscopic measurement analyses that are discussed in detail below, the visual image of Figure 1d confirms the synergistic action of the inhibitors (*Steel–WSS–Na₂HPO₄–MBT*), overcoming the defects and enhancing the advantages of the preceded separate use of MBT and Na₂HPO₄. After the exposure tests, a compact, resistant, uniform, protective layer was created, appearing to have a light-colored saline coating in the outer and a metallic gray or blackish inner layer, which is the magnetite layer. At a first glance, the lack of brown, reddish, and yellowish hues in the corrosion products incline us toward the conception that the main and more time-consuming corrosion processes were restricted successfully, resulting in a resistant and adherent protective layer on mild steel, which was almost intact after 96 h of subjection in a slightly saline environment and even after drying.

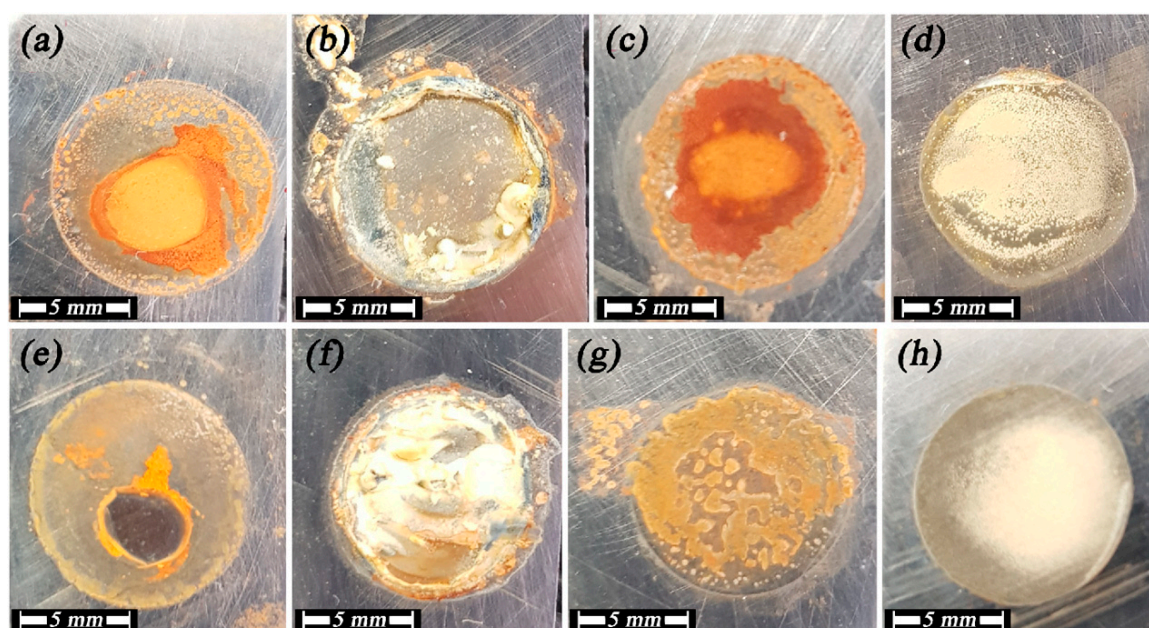


Figure 1. Visual images of mild steel after submission for 96 h: in WSS (a) *Steel–WSS–blank*, (b) *Steel–WSS–Na₂HPO₄*, (c) *Steel–WSS–MBT*, (d) *Steel–WSS–Na₂HPO₄–MBT*; in 3.5 wt % NaCl (e) *Steel–NaCl–blank*, (f) *Steel–NaCl–Na₂HPO₄*, (g) *Steel–NaCl–MBT*, (h) *Steel–NaCl–Na₂HPO₄–MBT*.

The mild steel visual pictures after exposure to 3.5 wt % NaCl for 96 h, in the presence or absence of inhibitors, are illustrated in Figure 1e–h. It can be seen that the surface of mild steel without the influence of inhibitors has lots of corrosion signs, as it is the bluish gray stain, indicating that uniform and local corrosion phenomena took place, with an accelerated rate regarding to the blank system (*Steel–NaCl–blank*, Figure 1e). On the other hand, corrosion products are also observed on the surface of both *Steel–NaCl–Na₂HPO₄* and *Steel–NaCl–MBT* (Figure 1f,g), reassuring that the chosen inhibitors are appropriate for the present system. Moreover, the surface of the sample with the presence of both inhibitors seems free from corrosion products in the outer area and a more compact, dark-colored adherent layer onto the metallic surface was developed, with brown-gray color, which was probably brown due to the organic tail of MBT and blackish/gray due to magnetite and/or wustite compounds, as will be discussed below (*Steel–NaCl–Na₂HPO₄–MBT*, Figure 1h) [45].

The SEM images of mild steel prior to exposure to electrolytes (*Steel–blank*) are illustrated in Figure 2. It can be seen that there are holes, dents, and scratches on the surface either due to the fabrication of the specimens or due to the cleaning process. Taking into account the EDS analysis, the iron value concentration was measured to be approximately 92.9 wt %, while the corresponding

oxygen value was estimated very low, roughly 0.1 wt % indicating the absence of iron oxide products (Table 3).

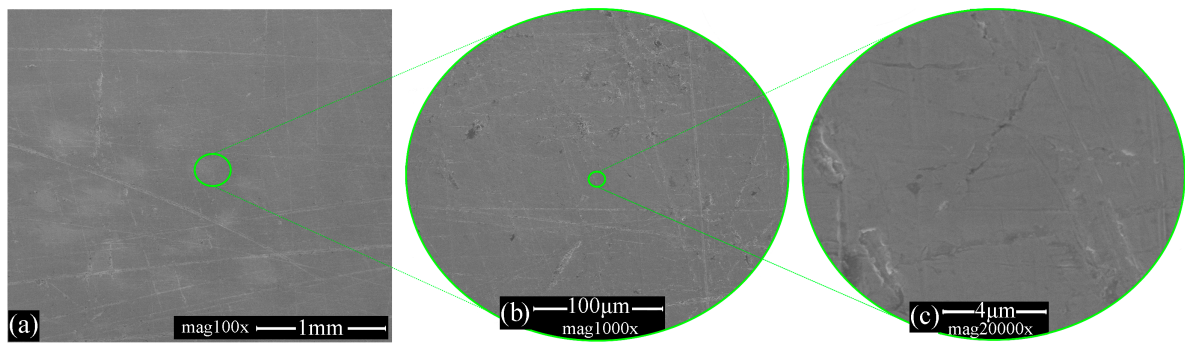


Figure 2. SEM images of mild steel prior exposure to electrolytes (*Steel-blank*).

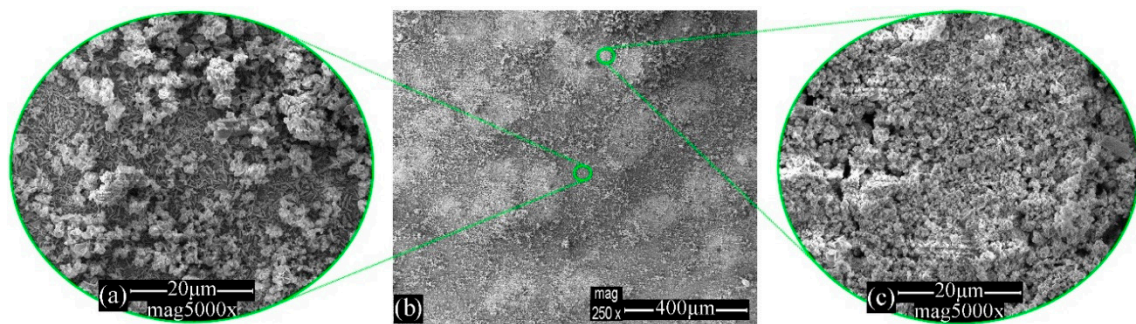


Figure 3. SEM images of mild steel immersed in WSS for 96 h in the absence of inhibitors.

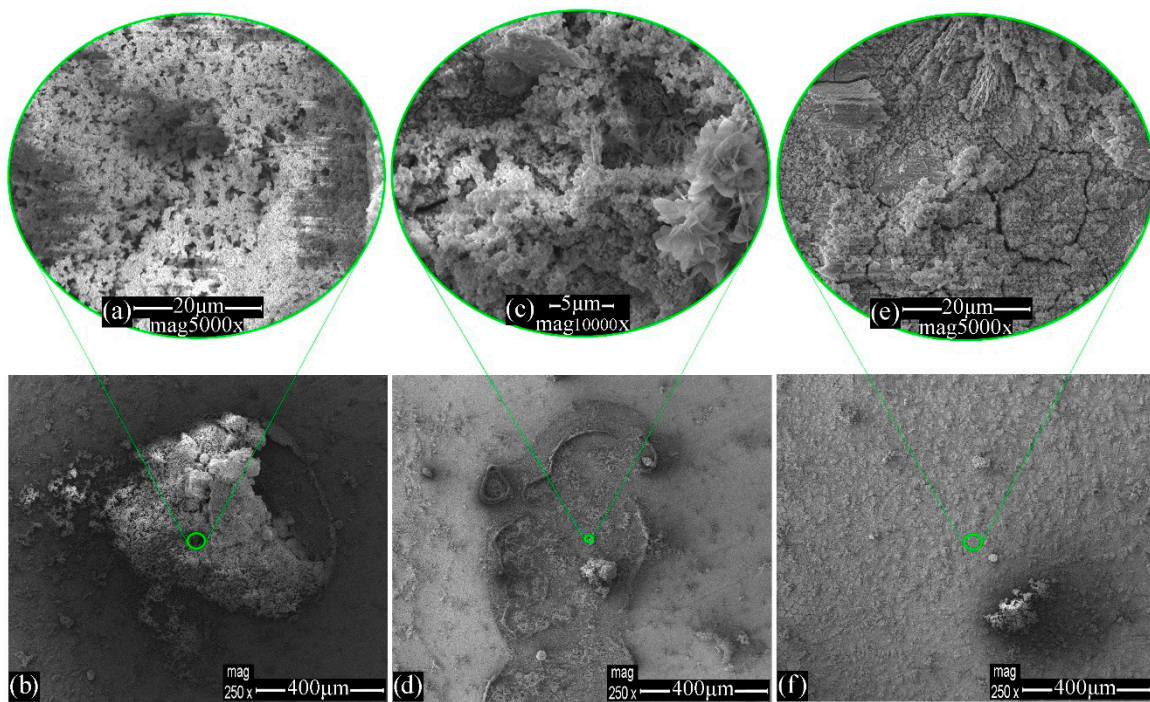


Figure 4. SEM images of mild steel immersed in WSS for 96 h in the presence of Na_2HPO_4 .

Table 3. Tabulated values of wt % element concentration of mild steel panels prior and after subjection in either WSS, or 3.5 wt % NaCl for 96 h in the presence of inhibitors or not.

Sample	Spectrum at	wt % Element Concentration						
		O	Fe	C	Si	P	S	Na
Steel-blank	Figure 2a	0.1	92.9	3.7	2.0	-	-	-
Steel-WSS-blank	Figure 3b	52.3	44.0	1.5	2.3	-	-	-
Steel-WSS-Na ₂ HPO ₄	Figure 4b	39.9	39.5	2.6	0.2	14.2	-	2.4
	Figure 4f	16.9	72.4	3.0	1.7	2.7	-	2.3
Steel-WSS-MBT	Figure 5e	44.6	46.1	4.2	1.2	-	3.6	-
	Figure 5f	44.4	46.9	4.3	1.5	-	2.9	-
Steel-WSS-Na ₂ HPO ₄ -MBT	Figure 6c	31.2	40.0	7.8	0.4	11.3	3.6	2.6
Steel-NaCl-Blank	Figure 7e	61.3	38.7	-	-	-	-	-
Steel-NaCl-Na ₂ HPO ₄	Figure 8b	39.3	39.0	3.0	0.3	14.9	-	-
	Figure 8d	35.5	49.9	3.3	0.1	6.5	-	3.0
Steel-NaCl-MBT	Figure 9b	23.0	67.4	4.7	1.5	-	2.2	-
Steel-NaCl-Na ₂ HPO ₄ -MBT	Figure 10b	47.1	26.8	4.5	-	16.0	5.2	0.4

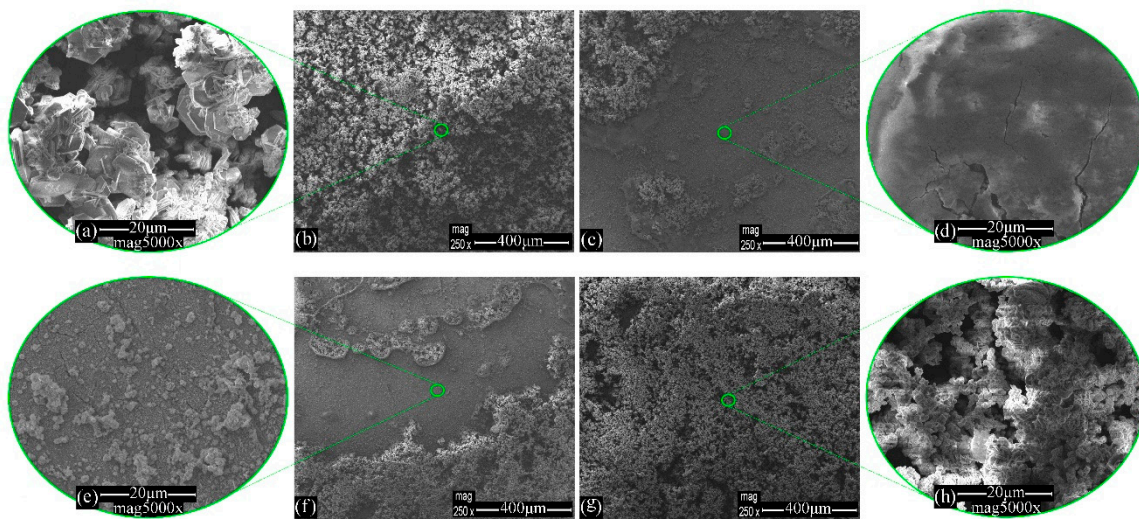


Figure 5. SEM images of mild steel immersed in WSS for 96 h in the presence of MBT.

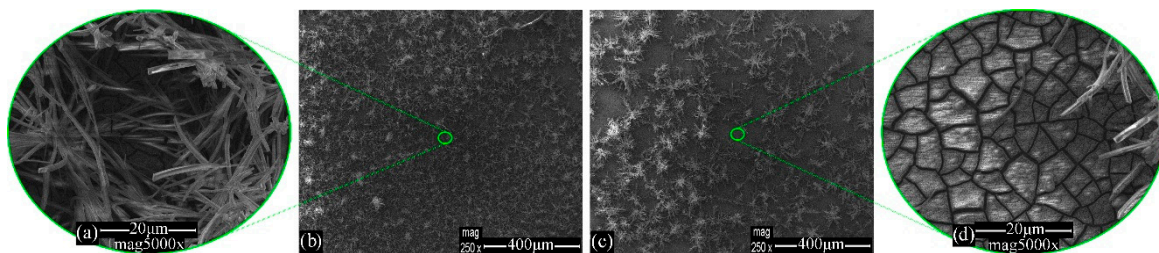


Figure 6. SEM images of mild steel immersed in WSS for 96 h in the presence of Na₂HPO₄ and 2-mecraptobenzothiazole (MBT).

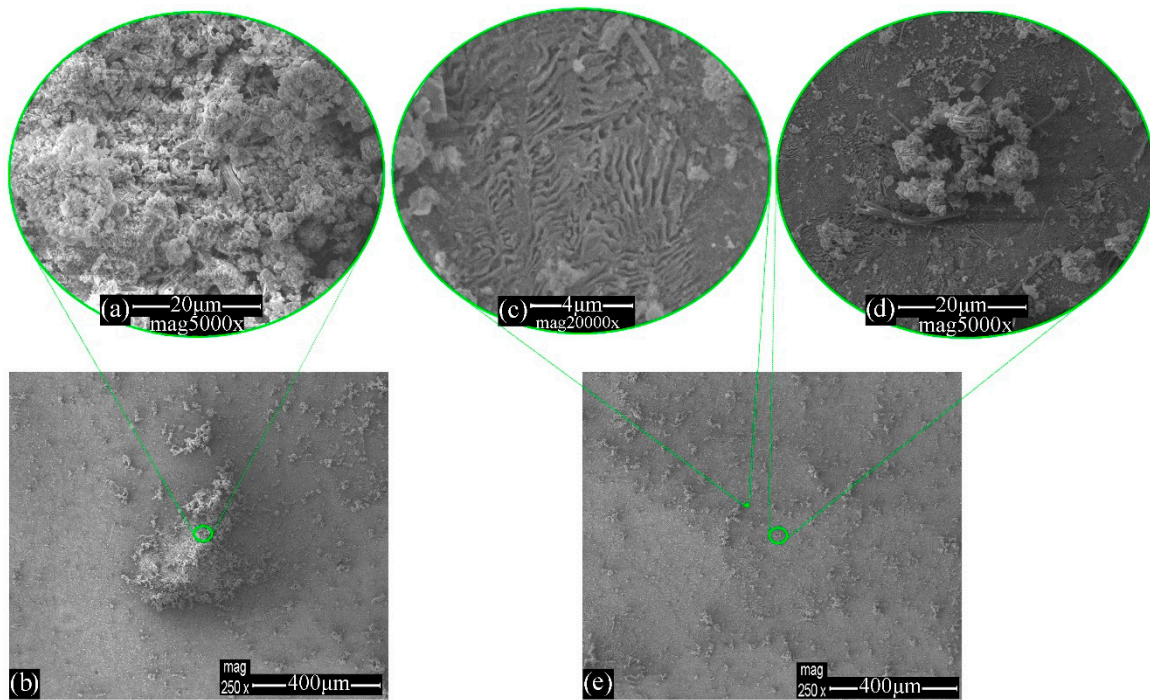


Figure 7. SEM images of mild steel immersed in 3.5 wt % NaCl for 96 h in the absence of inhibitors.

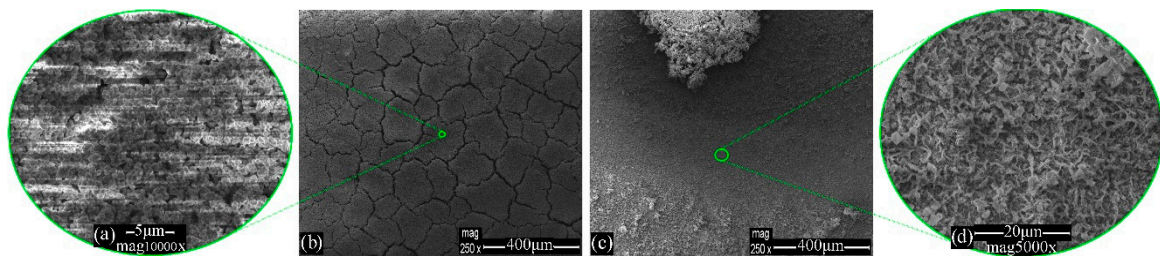


Figure 8. SEM images of mild steel immersed in 3.5 wt % NaCl for 96 h in the presence of Na_2HPO_4 .

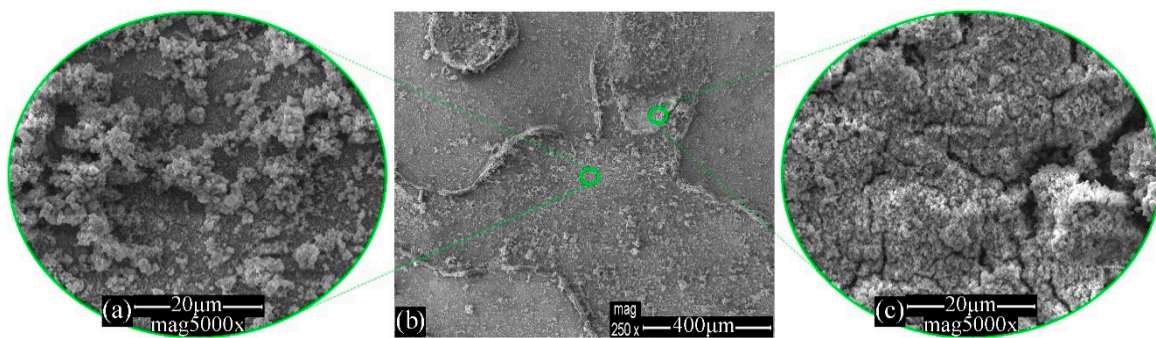


Figure 9. SEM images of mild steel immersed in 3.5 wt % NaCl for 96 h in the presence of MBT.

In general, the surface characterization of mild steel corrosion products remains a quite demanding issue, as denoted by previous works [46]. Various image analyzing techniques were deployed in order to assess the mild steel surface relating to its corrosion products structure and behavior after immersion in the studied inhibitor solutions.

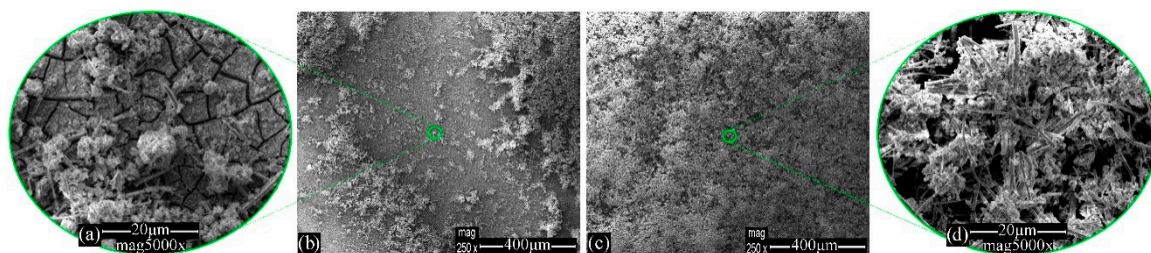


Figure 10. SEM images of mild steel immersed in 3.5 wt % NaCl for 96 h in the presence of Na_2HPO_4 + MBT.

In order to extract as much information as possible, it is a prerequisite to adopt a circumstantial model for the mild steel surface corrosion system during subjection in aquatic solutions, such as those proposed in the literature [7,47]. It is commonly accepted that the initial mixture of corrosion products consists of a primary viscous layer on a mild steel surface, to undergo afterwards gradation and separation into two distinguishable layers (an electrochemical double layer), an adherent rust layer, and a loosely adherent anodic oxide film [3,48]. At an early stage, amorphous masses of oxides with a spongy appearance are created, to transform primarily to lepidocrocite, part of which is further transformed in goethite. The studied phases have been generated either from the direct precipitation from a ferrous or a ferric solution, or by transformation of another iron oxide, at room temperature [3,49]. At a first glance at preceding investigations, Evan's model [50] regarding phase transition during wetting and drying conditions could contribute to illustrating the expended phase composition of a mild steel surface, after the prolonged exposure tests [51]. Consequently, during exposure, the reduction of lepidocrocite to a hydrated Fe^{2+} -intermediate takes place (phenomenon of olation) due to metal anodic dissolution, especially near the steel surface, where magnetite appears. However, oxidizing reactions can result in the emersion of lepidocrocite and maghemite phases [1,50,51] when oxygen circulation is evitable by drying [7].

The SEM images of mild steel immersed in WSS (*Steel–WSS–blank*) for 96 h, in the absence of inhibitors, are illustrated in Figure 3. Characteristic laminar morphologies of lepidocrocite were captured on the reference sample surface, exhibiting a large spectrum of more or less known crystalline formations, as it is denoted in the literature. Near the mild steel surface broken glass type [3], flowery and worm nest shapes dominate, in parallel with the gradual growth of miscellaneous laminar volumes of lepidocrocite formed radially outward from the metal surface. This particular formation is also described by many as cotton balls [3] and defined as crystalline phases due to the aggregation of flat grains of lepidocrocite grown on top of amorphous $\gamma\text{-Fe}_2\text{O}_3\cdot\text{H}_2\text{O}$ [46,48]. The EDS analysis of Figure 3b discloses enhanced oxygen value concentration compared to that of the *Steel–blank* sample due to the creation of the aforementioned iron oxides (Table 3).

The surface SEM images of *Steel–WSS–Na₂HPO₄* after subjection in WSS for 96 h are depicted in Figure 4. It can be seen that characteristic tassel-like structures, mainly consisting of $[\text{Fe}^{\text{II}}\text{-OH}]$ compounds, with substituted hydroxyls by phosphate anions (H_2PO_4^- , HPO_4^{2-} , PO_4^{3-}) [52], reveal the phosphates incorporation, thus making possible the identification of iron phosphates, appearing in amorphous or crystal phases. The latter are often observed as filamentous agglomerates [53] (Figure 4a,b). However, phosphorous detection through microscopy techniques of EDS analysis of the surface has been considered harsh, as phosphate anions get incorporated in steel crystal lattice [26]. Furthermore, ordinary structures of lepidocrocite spongy structure (and probably parts of maghemite, a phase that usually adopts the shape of its precursor [54]) and smaller aggregations of magnetite (as more globular, smooth) seem to be present, while a compact continuous inner layer (with cracks from drying process) has been obviously generated, which is indicative of steel surface passivation by phosphates (Figure 4c,d). In addition, large platy crystals of nanocrystalline phases are captured, reassuring the creation of the expected thin adherent passive layer of iron phosphates, maghemite, and lepidocrocite in crystalline and amorphous formations [26,53] (Figure 4e,f). It should be taken

into account that the special influence of phosphate anion is participating in various chemical paths. Although adsorbed phosphate is assumed to act as a precursor for hematite creation and often for goethite nucleation and growth, at different concentrations and especially at locally more basic areas, phosphate anions increase the negative electronic charge of ferrihydrite (present at earlier stages) between particles. Therefore, the formation of hematite retards or is limited [44]. Since the samples have undergone primary aging, in conjunction with the spectroscopic measurement results, it is considered that a part of the magnetite layer has decomposed in a binary solid-state transformation. At the same time, a structural conversion of magnetite, oxidizing partially to form maghemite and a compositional frontal transformation to hematite take place [55]. The choice of the physicochemical path that will be followed depends primarily on the anion concentration [56,57]. The EDS analysis of Figure 4b,f reveals elevated oxygen value concentrations compare to that of the sample *Steel-blank* due to the formation of the aforementioned iron oxides as well as the presence of phosphorus that is assigned to the adsorbed phosphates (Table 3).

Figure 5 pictures the surface SEM images of mild steel submitted to WSS for 96 h in the presence of MBT (*Steel-WSS-MBT*). It can be seen that hexagonal double-plates are illustrated, revealing the presence of magnetite [58], the precipitation of Fe^{2+} and Fe^{3+} ions from the solution, and the creation of green rust particles (general type $[\text{Fe}^{2+}_{(1-x)}\text{Fe}^{3+}_x(\text{OH})_2]^{x+}$) (Figure 5a,b). Positively charged ions from corroded iron forms sediments of double-hydroxide layers, consisting of coordinated Fe^{2+} and Fe^{3+} octahedra with hydroxylate groups between them [48,59]. Green rust acts as an ion exchange surface withholding other species of metal ions and decreasing locally the negative charge between the particles of the corrosion products, conferring more stability to the final layer [54,59]. Moreover, unattached geode type formations are present, enhancing the assumption of magnetite creation with smaller crystals of lepidocrocite inside the cavity, as the former is mostly detected near the metallic surface as a blackish oxide [58], while the latter usually constitutes the biggest part of the total corrosion products above (Figure 5c,d). Additionally, the creation of primarily small amounts of akaganeite [$\beta\text{-FeO}(\text{OH})$] is considered, whereas the precise identification of these phases was complicated using the SEM technique [46,47]. Taking into account the capture of cracks (Figure 5e,f), it may be remarked that a quite thick and compact inner layer was generated from the inhibitor (MBT) adsorption [29], in parallel with the conventional corrosion products of the mild steel, such as crystals of lepidocrocite and other aforementioned bulk structures of goethite, maghemite and lepidocrocite. The EDS analysis of Figure 5e,f discloses elevated oxygen value concentrations compared to that of the *Steel-blank* sample due to the formation of the aforementioned iron oxides as well as the presence of sulfur that is ascribed to the adsorbed organic MBT (Table 3).

The surface SEM images of mild steel immersed in WSS for 96 h in the presence of MBT together with Na_2HPO_4 (*Steel-WSS-Na₂HPO₄-MBT*) are demonstrated in Figure 6. Bulky corrosion products as tubular rods are predicting the creation of α and β phases of iron oxides, as well as more fine-grained phases of the expended corroded phases, as the interactivity of the mild steel with the inhibitors lessened the rate and the extent of the corrosion process (Figure 6a,b). The successful generation of a layer with cracks is probably due to the drying process, implying the conjunction of the organic inhibitor molecule (MBT) to a mild steel surface, as well as the formation of tertiary phosphates [26,60] (Figure 6c,d). The EDS analysis of Figure 6c reveals elevated oxygen value concentrations compared to that of the sample *Steel-blank* due to the creation of the aforementioned iron oxides along with the presence of sulfur and phosphorus elements that are attributed to the adsorbed organic MBT and inorganic phosphates, respectively (Table 3).

The surface SEM images of mild steel subjected to 3.5 wt % NaCl (*Steel-NaCl-blank*) for 96 h are illustrated in Figure 7. It can be seen that there is a surface distinctly damaged by the saline solution, with the characteristic appearance of an etched layer near the metal surface, as chloride anions accelerate corrosion phenomena (Figure 7a,b). In several areas, bigger bulk crystalline tubular or rod-like forms of goethite (often visually yellowish to reddish rust) or hematite (visually metallic gray rust) [54,61] and distinguishable cloud-like [3] lepidocrocite crystals are depicted (Figure 7c,e).

As commented in preceding studies, it seems that small amounts of goethite were formed after a significant exposure time [3] by lepidocrocite solid transformation due to the presence of chloride ions as well as by the transformation of green rust ($\text{Fe}^{\text{II}}_x\text{Fe}^{\text{III}}(\text{OH})_{3x+2y-z}(\text{A}^-)_z$ [54]) during the drying process (Figure 7d,e). The chloride ions, as aggressive anions, are considered [49] to accelerate the corrosion process, penetrating the protective layer and hence attacking the fresh unharmed metal surface beneath the layer, triggering pitting corrosion. Therefore, chloride anions may not be detected onto the corrosion product layer neither as ferrous (FeCl_2) nor as ferric (FeCl_3) salts, which are initially formed [47,62], since these salts are meant to be significantly soluble in water. The EDS analysis of Figure 7e reveals an elevated oxygen value concentration compared to that of the *Steel-blank* sample due to the formation of the previously mentioned iron oxides (Table 3).

The surface SEM images of *Steel-NaCl-Na₂HPO₄* after exposure in 3.5 wt % NaCl for 96 h are depicted in Figure 8. It seems that globular axially generated spongy agglomerations have constructed a quite homogenous voluminous layer, currently hindering the exposure of the inner layer on the metal surface. As mentioned before, these agglomerations are attributed to lepidocrocite, maghemite, and precursors of green rust (as magnetite) created in NaCl solution [15] and are not yet removed, due to the prolonged exposure process [3,63] (Figure 8a,b). Furthermore, miscellaneous laminas accreting in thorny three-dimensional structures [3] resemble hematite and goethite (sharper, more acicular) α phases with small aggregates of more globular lepidocrocite (or/and maghemite), which are precipitated during the submission together with tertiary phosphates [46,60,64] (Figure 8c,d). As mentioned before, cracks with diameters of a few micrometers are considered to be due to the drying stage (Figure 8b). The EDS analysis of Figure 8b,d reveals elevated oxygen value concentrations compare to that of the sample *Steel-blank* due to the formation of the aforementioned iron oxides as well as the presence of phosphorus, which is assigned to the adsorbed phosphates (Table 3).

The surface SEM images of mild steel immersed in 3.5 wt % NaCl for 96 h in the presence of MBT (*Steel-NaCl-MBT*) are demonstrated in Figure 9. Characteristic laminar and eroded rosettes of green rust, lepidocrocite, and hematite consist of the three-dimensional structures (Figure 9a), while the ruptured inner layer (Figure 9c) indicates the inhibitor (MBT) interaction with the steel surface [29,64,65]. The EDS analysis of Figure 9b reveals elevated oxygen value concentrations compared to that of the *Steel-blank* sample due to the creation of the previously mentioned iron oxides along with the presence of sulfur that is assigned to the adsorbed organic MBT (Table 3).

The surface SEM images of mild steel submitted to NaCl for 96 h in the presence of MBT together with Na_2HPO_4 (*Steel-NaCl-Na₂HPO₄-MBT*) are demonstrated in Figure 10. The accelerated corrosion test validates the aforementioned protective layer creation, in parallel with the emergence of both less and more fine-grained phases (tubular rods and laminar lepidocrocite and maghemite structures), attributing to the enhanced corroding environment in saline solution and to the prolonged submission process as well as to the formation of tertiary phosphates [26,60] (Figure 10). The EDS analysis of Figure 10b reveals elevated oxygen value concentrations compared to that of the *Steel-blank* sample due to the formation of the aforementioned iron oxides along with the presence of phosphorus and sulfur elements that are attributed to the adsorption of inorganic phosphates and organic MBT, respectively (Table 3).

3.2. Raman Spectroscopy Analysis

The Raman spectra of the mild steel panels after subsection to WSS for 96 h, in the presence of inhibitors or not, are depicted in Figure 11. The corresponding classification of the Raman spectra peaks is in Table S1. Regarding the *Steel-WSS-blank*, it can be mentioned that the region between 200 and 450 cm^{-1} of the Raman graph belongs to α , β , and γ -crystalline iron oxides and oxyhydroxides, accompanied with amorphous products, but is not considered as appropriate for the precise identification of the rust compounds (Figure 11a). Quite guardedly, it could be claimed that the pair of peaks near 225 and 290 cm^{-1} is assigned to the presence of hematite, the peak near 298 cm^{-1} is assigned to the presence of goethite, and that around 663 cm^{-1} is assigned to the presence

of magnetite [66]. The pair of peaks with the shoulders at about 1320 and 1630 cm^{-1} is attributed to ferrihydrites, which is the main iron oxyhydroxide rust compound of the present system [7].

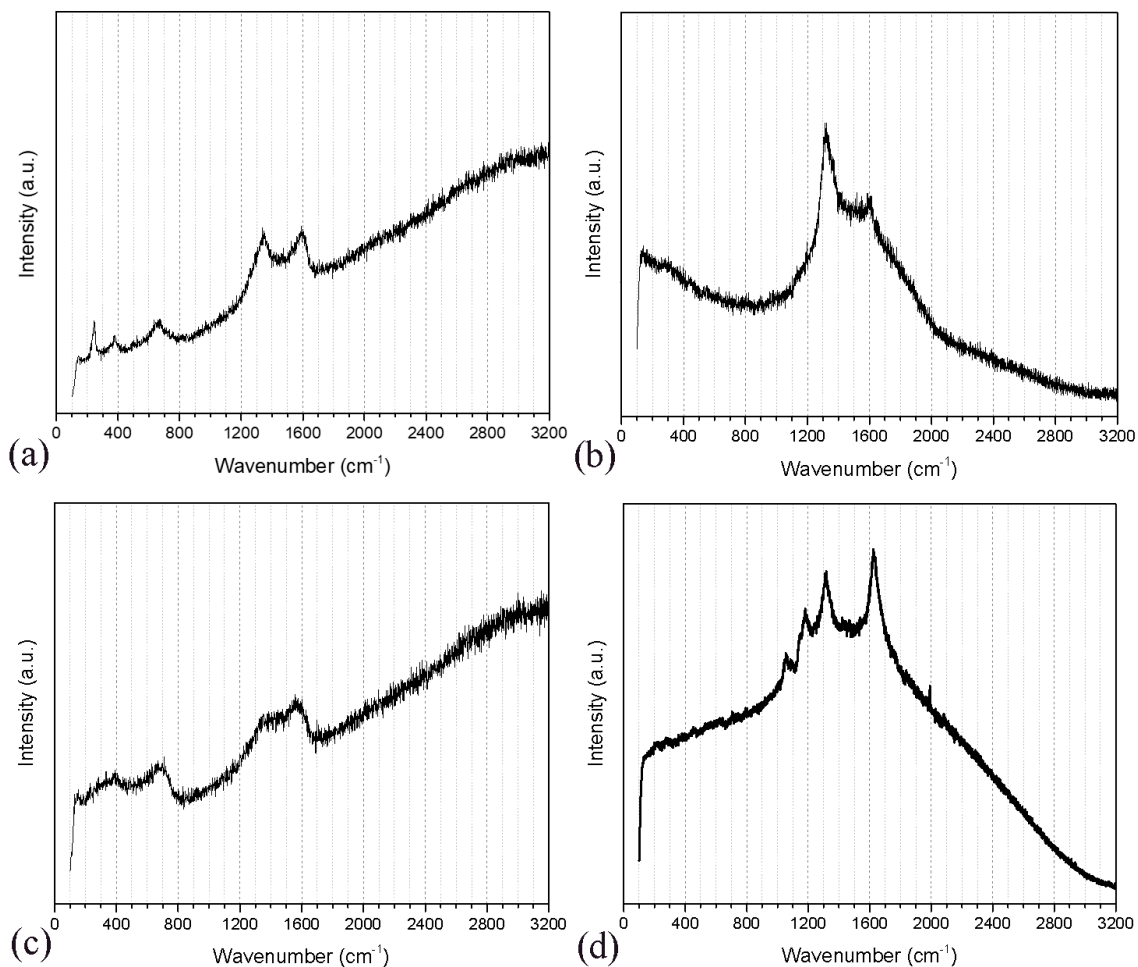


Figure 11. Raman spectra of the mild steel panels after subjection in WSS for 96 h: (a) *Steel-WSS-blank*, (b) *Steel-WSS-Na₂HPO₄*, (c) *Steel-WSS-MBT*, (d) *Steel-WSS-Na₂HPO₄-MBT*.

Taking into account the Raman spectrum of *Steel-WSS-Na₂HPO₄* (Figure 11b), it may be remarked that except for the initial noisy fluctuations from iron oxyhydroxides and oxides [63,67] or either from Fe–O lattice vibrations [68], the most intense peak at about 1310 cm^{-1} arrives from iron phosphate species and may be addressed to PO₂ asymmetric stretch [69], whereas the less intense (accompanied with a shoulder) near 1600 cm^{-1} could be attributed to bending vibrations of water molecules [68] attached to the more hygroscopic phases.

Considering the *Steel-WSS-MBT*, it can be mentioned that the organic inhibitor adsorption on [Fe–O–OH] species mitigated their characteristic Raman shifts, assuming that the elevated experimental line in the region 200–400 cm^{-1} implies their presence under MBT (Figure 11c). The two most discrete peaks were captured near 1380 cm^{-1} and 1590 cm^{-1} with a neck between them, which was a shifted pattern that was commented previously to emerge due to ferrihydrites. Furthermore, it could be claimed that the pair of peaks at 220 and 290 cm^{-1} with the detection of the primarily lower peak near 700 cm^{-1} is related to pyrite characteristic Raman shift, meaning the identification of the Fe–S band [70]. Enhancing this option, it should be considered that after drying at specific areas, the organic voluminous MBT molecule would be detected, hiding the rest, more crystalline structures underneath, whereas there would be sites where the organic layer would have been partially detached.

In view of the *Steel–WSS–Na₂HPO₄–MBT* Raman spectrum, it can be said that despite the fact that the first peak at 1050 cm⁻¹ seems to be attributed to bending vibrations of C–H bands of the MBT aromatic ring [65], its emergence in combination with the shoulder up to the next peak around 1185 cm⁻¹ and the smaller peak at 1316 cm⁻¹ reveal the identification of iron phosphate crystalline or amorphous compounds [69] (Figure 11d). The latter peak at 1628 cm⁻¹ is believed to correspond to the thione mode of the MBT molecule, which is indicative of being perpendicular to the metal surface orientation of the aromatic ring [65].

The Raman spectra of the mild steel panels after exposure to 3.5 wt % NaCl for 96 h, in the presence of inhibitors or not, are illustrated in Figure 12. Regarding the *Steel–NaCl–blank*, it can be mentioned that the generated thick three-dimensional amorphous corrosion products and the most dense and stable generated passive layer on the mild steel measured surface are considered to hinder the detection of the Raman shifts of more crystalline phases beneath (Figure 12a). Hence, the initial expected peaks of iron oxides and oxyhydroxides [67] are distorted due to the voluminous amorphous compounds. An intense peak at 1319 cm⁻¹ [63] is attributed to hematite (α -Fe₂O₃) and the less intense peak at 1593 cm⁻¹ [46] is attributed to (2-line) ferrihydrite (Fe₅HO₈·4H₂O), which makes its appearance between 1380 cm⁻¹ and 1600 cm⁻¹ [7].

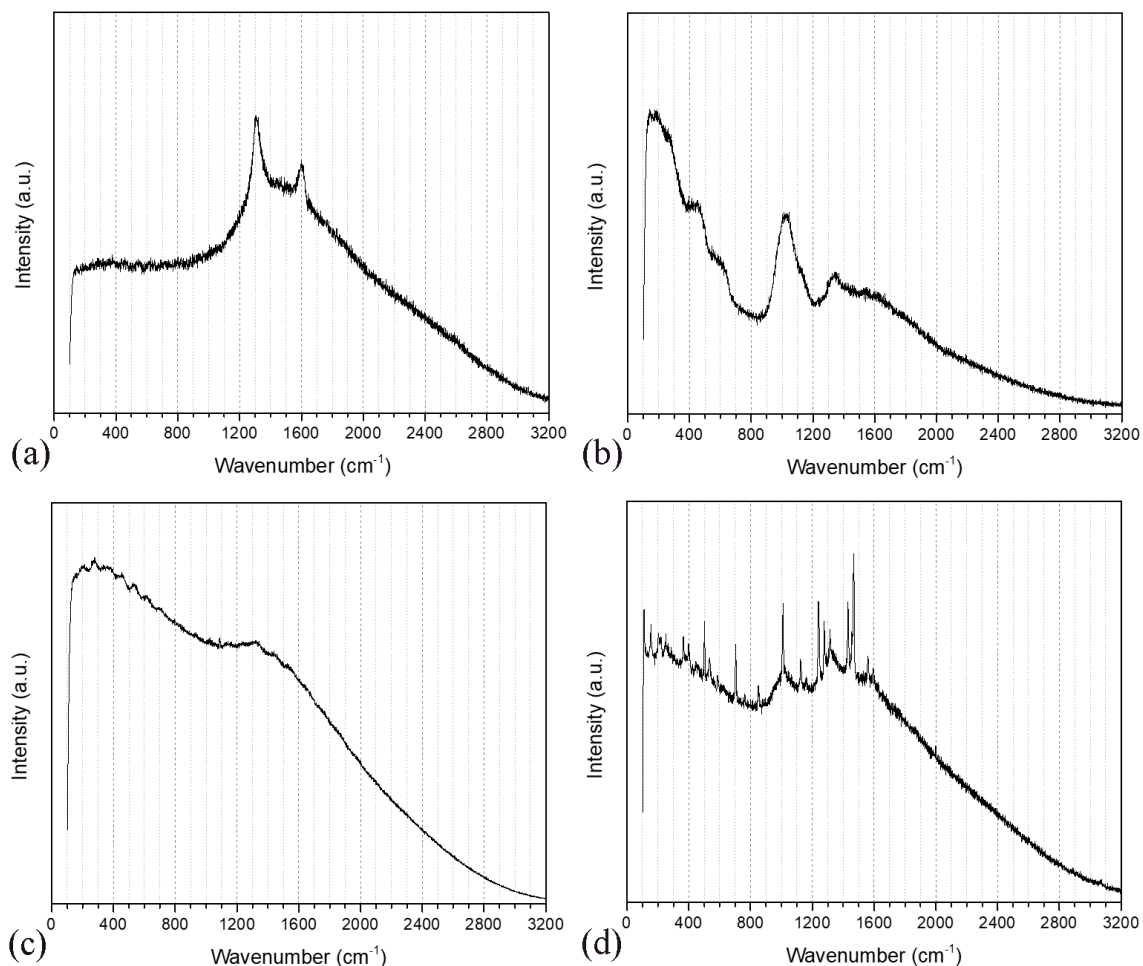


Figure 12. Raman spectra of the mild steel panels after subjection in 3.5 wt % NaCl for 96 h: (a) *Steel–NaCl–blank*, (b) *Steel–NaCl–Na₂HPO₄*, (c) *Steel–NaCl–MBT*, (d) *Steel–NaCl–Na₂HPO₄–MBT*.

Taking into account the Raman spectrum of *Steel–NaCl–Na₂HPO₄* (Figure 12b), it may be remarked that the absence of a peak near 218–221 cm⁻¹, which is attributed in the literature to the symmetric stretch of interlayer chloride ions in green rust [63,68] in combination with the detection of iron

phosphate salts vibrations, at 430–450 cm^{-1} for $\text{Fe}_4(\text{P}_2\text{O}_7)_3$ and at 1011 cm^{-1} for a symmetric PO_3^{2-} symmetric stretch of $\text{Fe}_3(\text{PO}_4)_2\text{A}$ (A for anion) [69], reassures mild steel surface phosphating and consequently the increase of crystallinity in corrosion products after exposure and drying processes.

Considering the *Steel–NaCl–MBT* (Figure 12c), it can be noticed that although low wavenumbers of Raman shift are connected with iron oxides as commented, the differentiation of mild steel spectrum enhances the surmise of MBT physical and chemical adsorption, which is in accordance with the absence of other characteristic peaks of MBT, as at 717 cm^{-1} , 1013 cm^{-1} , 1564 cm^{-1} , and 1593 cm^{-1} . The strongest peak near 278 cm^{-1} in conjunction with noisy, less intense peaks at 350 cm^{-1} , 470–480 cm^{-1} , 530–540 cm^{-1} , and 610 cm^{-1} reveal the generation of the Fe–S bond [71]. A less intense but relatively obvious peak obtained near 1320 cm^{-1} is connected to the N = C–S ring stretching mode, with its intensity considered in the literature as proportionate to the inhibitor chemisorption progress [71]. The peak at 1395 cm^{-1} is considered to stem from stretching vibrations of the C–C band in the aromatic ring of MBT [65].

In view of the *Steel–NaCl–Na₂HPO₄–MBT* (Figure 12d), it can be said that a more clarifying Raman spectrum with more than 15 Raman shift peaks was gained under accelerating corrosion conditions, as there are in the saline solution. The smaller peaks near 300 cm^{-1} (shoulder) and 400 cm^{-1} in addition to those near 500 cm^{-1} and 530 cm^{-1} are assumed to be caused by Fe–S generated by the chemisorption of MBT on the surface of the sample [71]. The peak that arises near 700 cm^{-1} may be attributed to P–O–P symmetric stretch vibrations, taking into account the simultaneous appearance of a smaller peak near 850 cm^{-1} generated by $[\text{HPO}_4]^{-2}$ anion symmetric stretch [54,63]. The next pair of Raman shifts near 1000 cm^{-1} (shoulder) and 1120 cm^{-1} comes to identify iron phosphate crystalline or amorphous phases [69] in conjunction with the combination of two other shifts near 1250 cm^{-1} and 1270 cm^{-1} and a smaller shift at 1310 cm^{-1} , the latter of which may have been gained from PO_2 asymmetric stretch. Moreover, the pair of 1430 cm^{-1} and 1480 cm^{-1} peaks in combination with those at 1580 cm^{-1} and 1590 cm^{-1} were noted to be in accordance with experimental Raman shift values for the adsorbed MBT molecule, especially when it is measured in its thione mode [65,72].

3.3. X-ray Diffraction Analysis

The XRD patterns of the mild steel panels after subjection in WSS for 96 h in the presence or absence of the evaluated corrosion inhibitors are depicted in Figure 13. The collected XRD spectra reveal that the exposure of the mild steel panels to WSS + Na_2HPO_4 leads to the detection of XRD diffraction peaks corresponding to [65-4899 Fe iron], [30-0662 $\text{Fe}_3(\text{PO}_4)_2 \cdot 8\text{H}_2\text{O}$ vivianite, syn], [01-074-5846 $\text{Fe}_{0.96}\text{P}_{0.04}$ iron phosphide], goethite [$\alpha\text{-FeO}(\text{OH})$], and lepidocrocite [$\gamma\text{-FeO}(\text{OH})$] [73] (Figure 13b). Moreover, the same diffraction peaks are detected via the exposure of mild steel panels to WSS in the presence of Na_2HPO_4 and MBT (Figure 13d). Furthermore, the exposure of mild steel panels to WSS in the absence or presence of MBT leads to the verification of XRD diffraction peaks that are attributed to [65-4899 Fe Iron], goethite [$\alpha\text{-FeO}(\text{OH})$], and lepidocrocite [$\gamma\text{-FeO}(\text{OH})$] (Figure 13a,c).

The mild steel specimen surfaces after subjection in 3.5 wt % NaCl for 96 h were also analyzed by XRD to determine the crystal structure (Figure 14). XRD diffraction peaks corresponding to [65-4899 Fe iron], [30-0662 $\text{Fe}_3(\text{PO}_4)_2 \cdot 8\text{H}_2\text{O}$ vivianite, syn], [01-074-5846 $\text{Fe}_{0.96}\text{P}_{0.04}$ iron phosphide], goethite [$\alpha\text{-FeO}(\text{OH})$], and lepidocrocite [$\gamma\text{-FeO}(\text{OH})$] are ascertained after the exposure of mild steel panels to 3.5 wt % NaCl in the presence of either Na_2HPO_4 (Figure 14b) or Na_2HPO_4 along with MBT (Figure 14d) [73]. Finally, the submission of the mild steel panels in 3.5 wt % NaCl in the absence or presence of MBT leads to the verification of XRD diffraction peaks that are attributed to [65-4899 Fe iron], goethite [$\alpha\text{-FeO}(\text{OH})$], and lepidocrocite [$\gamma\text{-FeO}(\text{OH})$] (Figure 14a,c). According to the literature [74], vivianite is a common and complicated breakdown product of the interaction of phosphate, iron, and H_2O .

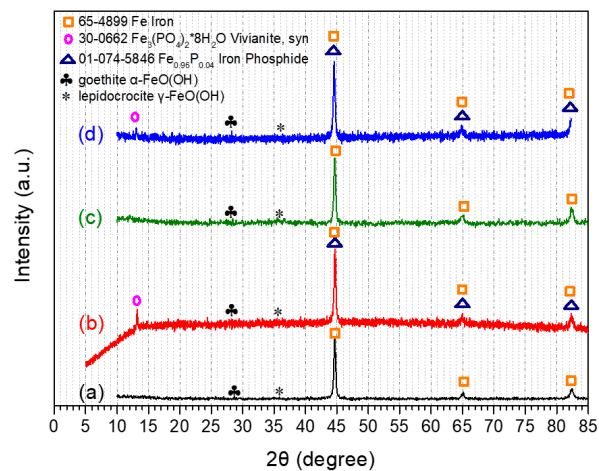


Figure 13. XRD spectra of the mild steel panels after submission in WSS for 96 h: (a) *Steel–WSS–blank*, (b) *Steel–WSS–Na₂HPO₄*, (c) *Steel–WSS–MBT*, (d) *Steel–WSS–Na₂HPO₄–MBT*.

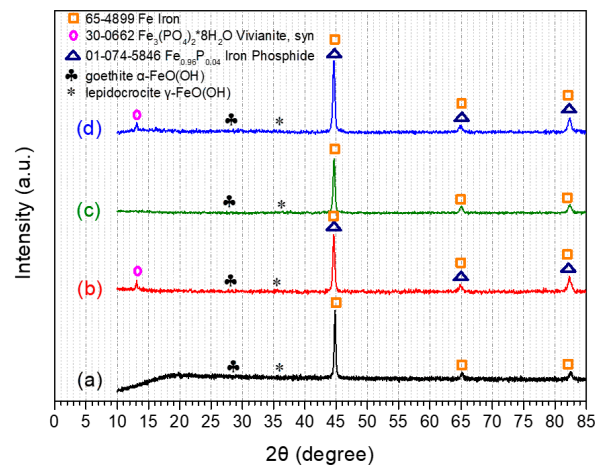


Figure 14. XRD spectra of the mild steel panels after submission in 3.5 wt % NaCl for 96 h: (a) *Steel–NaCl–blank*, (b) *Steel–NaCl–Na₂HPO₄*, (c) *Steel–NaCl–MBT*, (d) *Steel–NaCl–Na₂HPO₄–MBT*.

3.4. Electrochemical Studies

All the EIS, PP, and LPR electrochemical characterizations were performed in a pH range from 7.33 to 7.97 (Table 2). It should be taken into consideration that all the electrochemical measurements were conducted in triplicate, and a corresponding representative curve is illustrated for each sample.

In general, the presence of a compound into an electrolyte solution can shift the OCP either into positive values if the compound reacts as an anodic inhibitor retarding the oxidation process, or into negative values if the compound inhibits the cathodic reactions. The observation of the OCP values in respect of the time can provide information related to the stability of the electrolytic system in order for linear sweep voltammetry characterizations such as PP to be conducted.

Taking into account the evolution of OCP versus time in the case of mild steel panels after subjection in WSS for 23 h at room temperature (Figure 15), it is observed that the system including the mild steel together with the phosphates (*Steel–WSS–Na₂HPO₄*) shifts the OCP to more positive values after the fourth hour compared to the one of the *Steel–WSS–blank*. This indication clearly denotes that Na_2HPO_4 acts as an anodic inhibitor for mild steel, which is a result that is also confirmed by the literature [75]. On the other hand, for the system *Steel–WSS–MBT*, the OCP shifts to negative values, indicating that the presence of MBT inhibits the cathodic reactions [76]. Finally, the presence of both Na_2HPO_4 and MBT into the WSS (*Steel–WSS–Na₂HPO₄–MBT*) results in OCP values more negative

than those of *Steel–WSS–blank* and more positive than those of *Steel–WSS–MBT*. This behavior can be assigned to the simultaneous inhibition of the cathodic reactions as well as to the formation of a protective layer that inhibits the anodic reactions. Moreover, it can be mentioned that during the beginning of exposure (0–2 h), the corrosion potential (OCP) is lower than in isolated inhibitor systems due to passivation, but as the exposure time elapses, the OCP increases up to an almost stable moderate value for many hours. This behavior is characteristic of the accelerated formation of metastable pits at first and the gradual passivation of all of them, up to the restoration of the passive layer and the return of the system to the initial OCP, which is a process known as re-passivation [77].

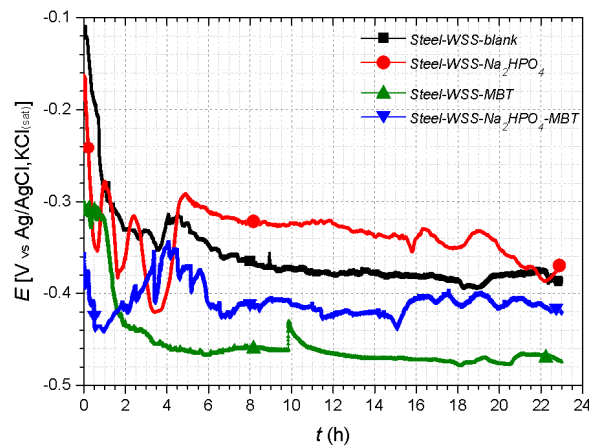


Figure 15. The evolution of open circuit potential (OCP) versus time in case of the mild steel panels after submission in WSS for 23 h: (■ filled square) *Steel–WSS–blank*, (● filled circle) *Steel–WSS–Na₂HPO₄*, (▲ filled triangle) *Steel–WSS–MBT*, (▼ filled triangleU) *Steel–WSS–Na₂HPO₄–MBT*.

Considering the evolution of OCP versus time in the case of the mild steel panels after subjection in 3.5 wt % NaCl for 23 h at room temperature (Figure 16), it can be noticed that the presence of Na₂HPO₄ and MBT in the electrolytic solutions increases the OCP compared to the *Steel–NaCl–blank*. These facts denote that there is an inhibition to the anodic reactions resulting in the corrosion protection of the mild steel. The increase in potential is assigned to the creation of protective films onto the metal surface, making it more resistant to corrosion than the panel subjected to the solution without inhibitor additives. Moreover, it may be remarked that MBT acts as a mixed inhibitor for mild steel in NaCl solutions [78].

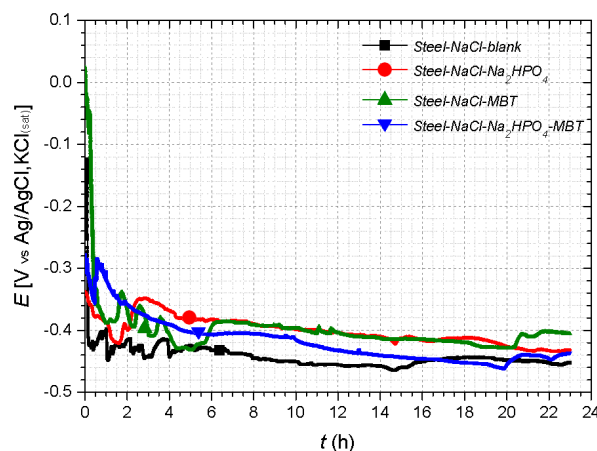


Figure 16. The evolution of OCP versus time in case of the mild steel panels after submission in 3.5 wt % NaCl for 23 h: (■ filled square) *Steel–NaCl–blank*, (● filled circle) *Steel–NaCl–Na₂HPO₄*, (▲ filled triangle) *Steel–NaCl–MBT*, (▼ filled triangleU) *Steel–NaCl–Na₂HPO₄–MBT*.

The polarization curves recorded for mild steel panels in the presence or absence of inhibitors after subjection in WSS for 24 h are demonstrated in Figure 17. Considering the cathodic branches of the diagram (Figure 17a), it can be seen that the presence of MBT into the solution (*Steel–WSS–MBT*) results to the appearance of lower cathodic current densities compared to the *Steel–WSS–blank*, indicating a possible reduction of the cathodic reactions. On the other hand, according to the same diagram, there is no evidence that the other two systems (*Steel–WSS–Na₂HPO₄*, *Steel–WSS–Na₂HPO₄–MBT*) affect the cathodic reactions. Taking into account the anodic branches of the polarization curves (Figure 17b), it may be remarked that the addition of Na₂HPO₄ into the commensurate solution retards the anodic reactions effectively, since the corresponding anodic current densities are decreased compared to those of the *Steel–WSS–blank*. On the contrary, there is no indication that the *Steel–WSS–MBT* and *Steel–WSS–Na₂HPO₄–MBT* systems influence the anodic reactions.

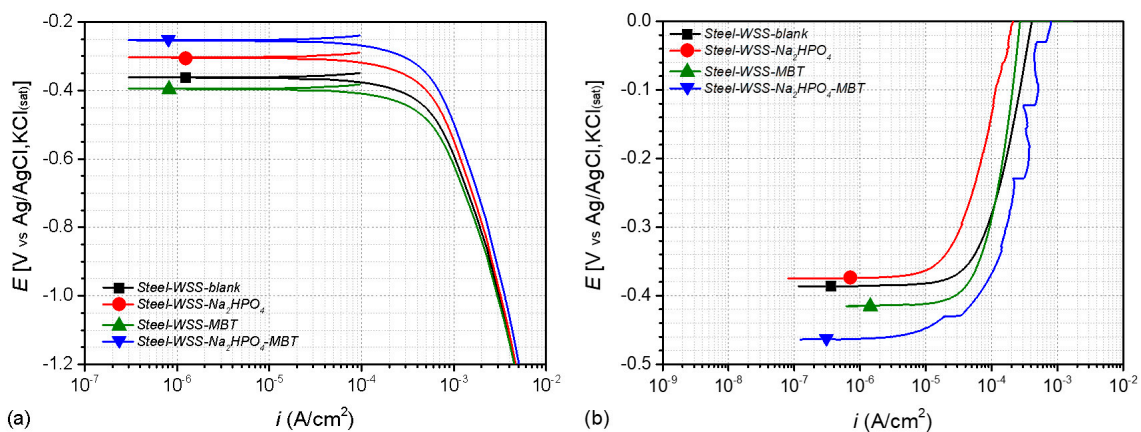


Figure 17. The polarization curves (a) cathodic, (b) anodic, recorded for mild steel panels after submission in WSS for 24 h: (■ filled square) *Steel–WSS–blank*, (● filled circle) *Steel–WSS–Na₂HPO₄*, (▲ filled triangle) *Steel–WSS–MBT*, (▼ filled triangle) *Steel–WSS–Na₂HPO₄–MBT*.

Furthermore, studying the cathodic branches of the polarization curves recorded for mild steel panels in the presence or absence of inhibitors after subjection in 3.5 wt % NaCl for 24 h, it is mentioned that the addition of Na₂HPO₄ either alone or in combination with MBT affected the cathodic reactions by lowering the corresponding cathodic current densities (Figure 18a). Therefore, there is an indication of a possible reduction of the cathodic reactions for both the *Steel–NaCl–Na₂HPO₄*, and *Steel–NaCl–Na₂HPO₄–MBT* systems. Considering the anodic branches, it could be documented that the introduction of the inhibitors suppresses the anodic reactions because of the reduction of the correlative anodic corrosion current densities (Figure 18b). This outcome can be attributed to the formation of corresponding protective layers.

Taking into account the Pourbaix diagram of iron [79], it may be remarked that in all the PP characterizations, reductions of both water and oxygen take place because the PP measurements were conducted in a pH range from 7.33 to 7.97 (Table 2) as well as the cathodic and anodic branches of polarization curves being recorded in a potential range between -1.6 V and 0 V versus Ag/AgCl, KCl(sat) electrode. Furthermore, in the aforementioned ranges of pH and potential, dissolution of iron exists but, be that as it may, the oxidation of iron does not involve the oxidation of water. In addition, it should be taken into consideration that the PP characterization technique was used only for qualitative interpretations, because the calculation of both the corrosion current (i_{corr}) and R_p values via the linear fitting of the polarization curves according to the Tafel method is not feasible, due to the existence of two reduction processes in the system: the reduction of water and the reduction of oxygen [80]. Moreover, the corrosion current density cannot be determined from the anodic branches, as there is no clear linear region. Finally, under the aforementioned experimental conditions, steel is also corroded via localized corrosion with the formation of pits [81,82]. Therefore, the Tafel method is not appropriate

to be used for localized corrosion, such as pitting corrosion, as it only yields an average uniform corrosion rate [83].

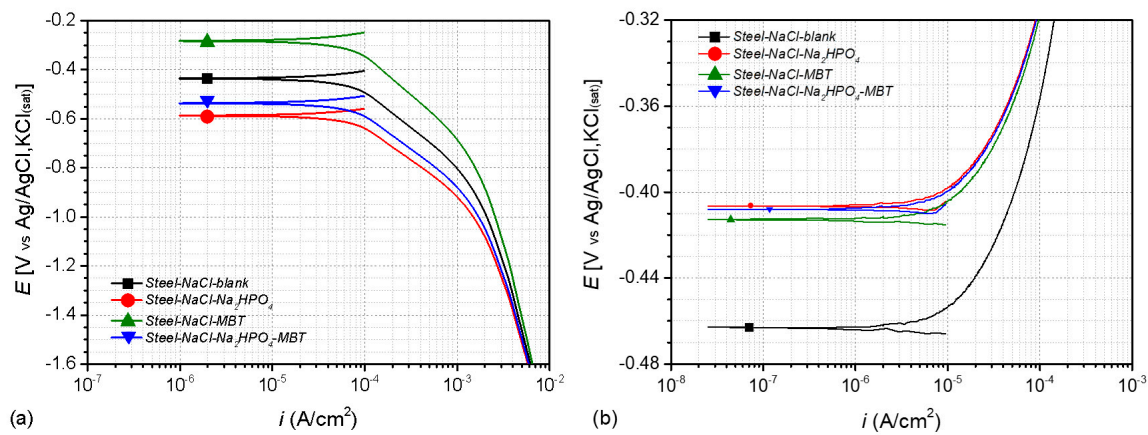


Figure 18. The polarization curves (a) cathodic and (b) anodic, recorded for mild steel panels after submission in 3.5 wt % NaCl for 24 h: (■ filled square) *Steel-NaCl-blank*, (● filled circle) *Steel-NaCl-Na₂HPO₄*, (▲ filled triangle) *Steel-NaCl-MBT*, (▼ filled triangle) *Steel-NaCl-Na₂HPO₄-MBT*.

Regarding the LPR measurements, it can be noted that all the mild steel panels were exposed to either WSS or 3.5 wt % NaCl for 96 h, in the presence of inhibitors or not. Bearing in mind the obtained R_p values (Table 4), it can be assumed that the presence of both Na_2HPO_4 and MBT in the electrolytic solutions has as an outcome enhanced corrosion protection of mild steel, as the *Steel-WSS-Na₂HPO₄-MBT* and *Steel-NaCl-Na₂HPO₄-MBT* systems exhibit R_p values higher compared to either the systems without inhibitors (*Steel-WSS-blank* and *Steel-NaCl-blank*) or to those systems including only one inhibitor.

Table 4. Tabulated values of E_{OC} [V vs. Ag/AgCl, KCl(sat)] obtained from the potentiodynamic polarization (PP) technique and of R_p estimated via the linear polarization resistance (LPR) method acquired for all mild steel panels after subjection in either WSS or 3.5 wt % NaCl in the presence of inhibitors or not.

Sample	E_{OC} (V) (Cathodic Branch) (24 h Exposure)	E_{OC} (V) (Anodic Branch) (24 h Exposure)	R_p (Kohm cm ²) (96 h Exposure)
<i>Steel-WSS-blank</i>	-0.361	-0.386	6.279
<i>Steel-WSS-Na₂HPO₄</i>	-0.303	-0.374	2.852
<i>Steel-WSS-MBT</i>	-0.394	-0.415	4.731
<i>Steel-WSS-Na₂HPO₄-MBT</i>	-0.253	-0.463	6.730
<i>Steel-NaCl-blank</i>	-0.435	-0.462	2.822
<i>Steel-NaCl-Na₂HPO₄</i>	-0.586	-0.406	1.800
<i>Steel-NaCl-MBT</i>	-0.282	-0.412	3.132
<i>Steel-NaCl-Na₂HPO₄-MBT</i>	-0.536	-0.408	4.054

The EIS plots of mild steel panels in the presence or absence of inhibitors after subjection in WSS are demonstrated in Figure 19. Taking into account the EIS Bode curves after 24 h of exposure (Figure 19a), it can be seen that the *Steel-WSS-Na₂HPO₄* and *Steel-WSS-Na₂HPO₄-MBT* systems illustrate higher EIS moduli compared to the one of the *Steel-WSS-blank*, indicating that the presence of the Na_2HPO_4 inhibitor alone or together with MBT into the corrosive environment increases the mild steel corrosion protection. On the contrary, the addition of an MBT compound into the WSS solution does not seem to improve the corrosion protection of the mild steel. Regarding the EIS Bode curves obtained after 96 h of exposure to WSS (Figure 19b), the same results are observed denoting

that the introduction of the Na_2HPO_4 inhibitor alone or together with MBT in to the WSS solution protects the mild steel from corrosion.

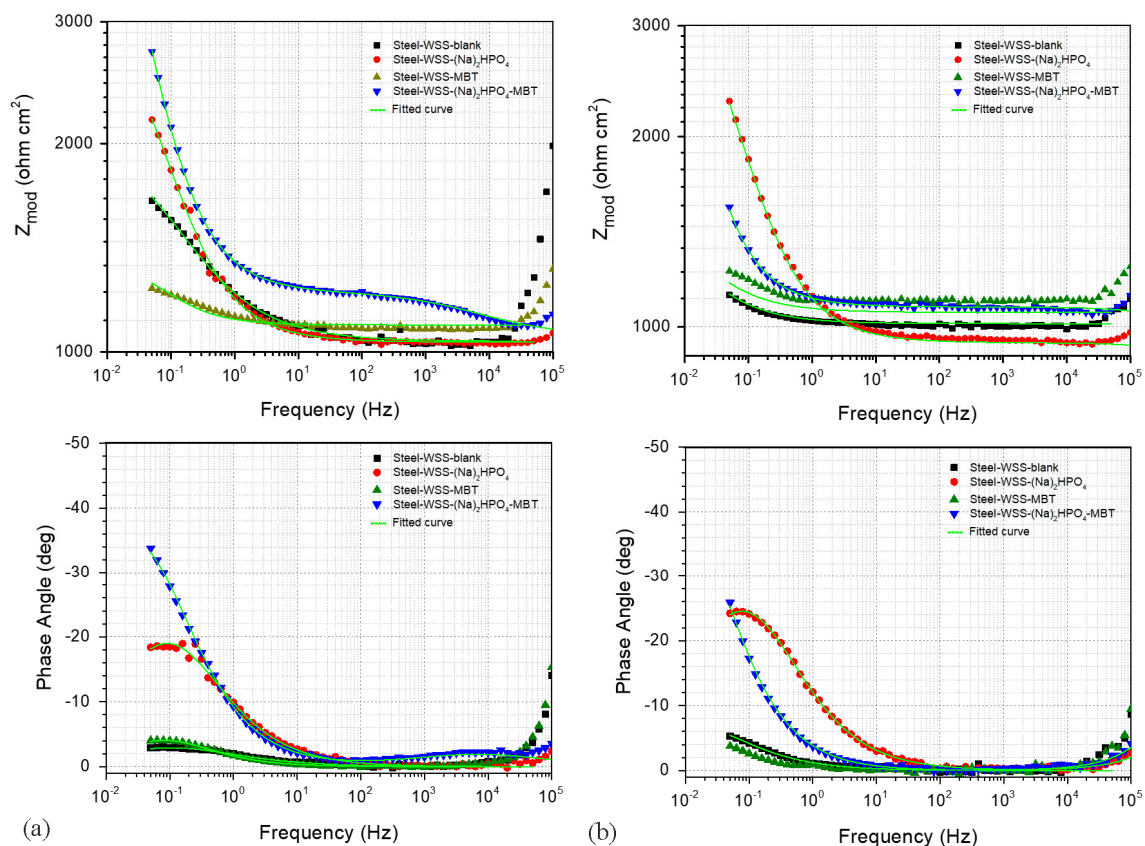


Figure 19. Electrochemical impedance spectroscopy (EIS) plots recorded for mild steel panels after submission in WSS for (a) 24 h and (b) 96 h: (■ filled square) *Steel-WSS-blank*, (● filled circle) *Steel-WSS- Na_2HPO_4* , (▲ filled triangle) *Steel-WSS-MBT*, (▼ filled triangle) *Steel-WSS- Na_2HPO_4 -MBT*, (—) Fitted curve.

Considering the EIS plots of mild steel panels in the presence or absence of inhibitors after subjection in 3.5 wt % NaCl (Figure 20), it is clearly seen that after 24 h of exposure (Figure 20a), the system *Steel-NaCl- Na_2HPO_4 -MBT* illustrates the highest EIS modulus in the low-frequency range, denoting that the presence of the Na_2HPO_4 inhibitor in accordance with MBT into the corrosive environment increases the mild steel corrosion protection. On the other hand, the insertion of either Na_2HPO_4 or MBT compounds into the 3.5 wt % NaCl electrolytic solution does not remarkably improve the corrosion protection of the mild steel. In view of the EIS Bode curves acquired after 96 h of exposure to 3.5 wt % NaCl (Figure 20b), it may be remarked that the addition of Na_2HPO_4 inhibitor alone or together with MBT into the electrolytic solution protects the mild steel from corrosion.

The EIS Bode plots for both the untreated mild steel and the systems including MBT (*Steel-WSS-MBT*, *Steel-NaCl-MBT*) after exposure to either WSS or 3.5 wt % NaCl for 24 h can be described with one time constant in the middle–low-frequency range that is attributed to the corrosion process (Figures 19 and 20). However, as corrosion progresses from 24 h to 96 h, the relative relaxation process moves to lower frequencies because of the increase of the corrosion active area and the corresponding double-layer capacitance enhancement.

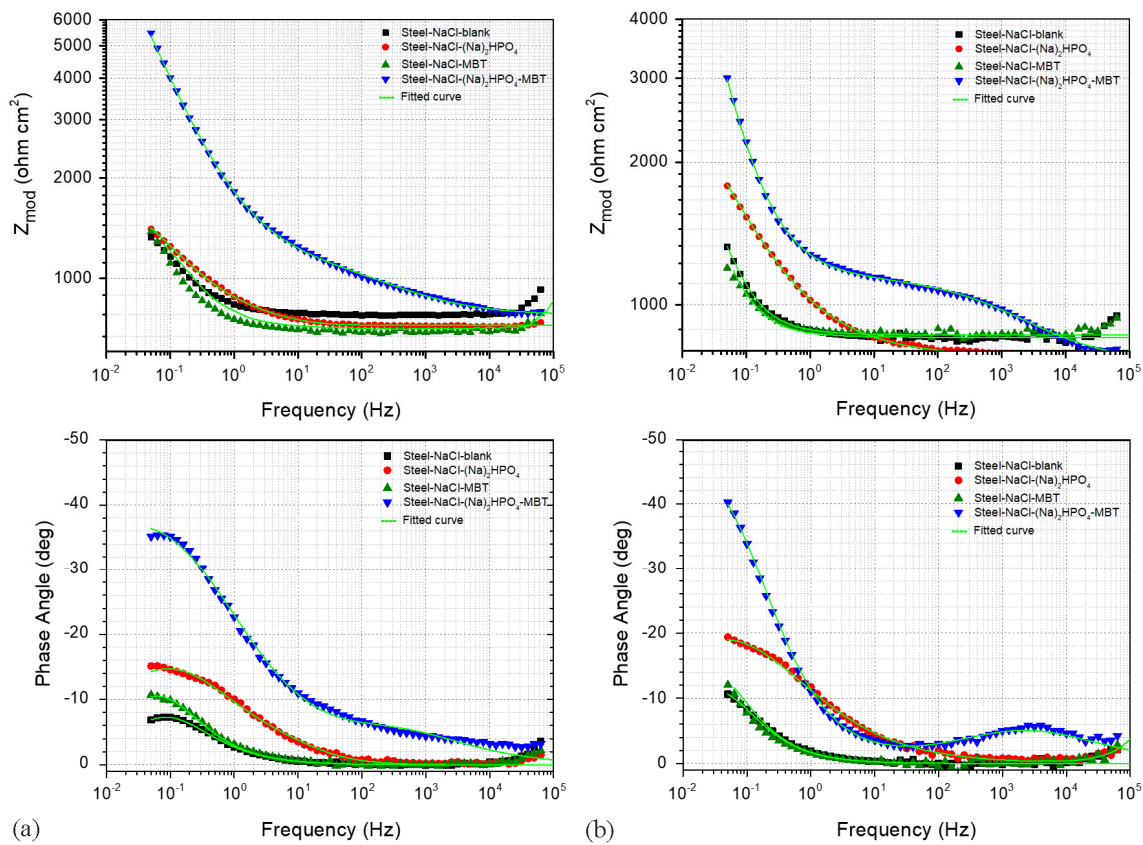


Figure 20. EIS plots recorded for mild steel panels after submission in 3.5 wt % NaCl for (a) 24 h and (b) 96 h: (■ filled square) *Steel-NaCl-blank*, (● filled circle) *Steel-NaCl-Na₂HPO₄*, (▲ filled triangle) *Steel-NaCl-MBT*, (▼ filled triangleU) *Steel-NaCl-Na₂HPO₄-MBT*, (–) Fitted curve.

On the other hand, estimating the EIS Bode plots for the systems including both Na₂HPO₄-MBT or only Na₂HPO₄ in either WSS or 3.5 wt % NaCl for 24 h, it can be noted that two time constants are illustrated: one in the high-middle frequency range that is ascribed to a film formation between the mild steel surface and the phosphate compounds, and a second one in the middle-low-frequency range that is assigned to corrosion process (Figures 19 and 20). As the exposure time elapses from 24 h to 96 h, the time constant assigned to corrosion process is shifted to lower frequencies due to the enhancement of the corrosion area and the corresponding double-layer capacitance increment.

The interpretation of the obtained EIS results for the mild steel panels after subsection in the electrolytic solutions in the absence or presence of corrosion inhibitors was conducted by numerical fitting using the equivalent circuits depicted in Figure 21. According to these equivalent circuits, the pure capacitors have been replaced by constant phase elements (CPE). This adaptation is mandatory when the phase shift of a capacitor is different from -90° [84]. The impedance of an R-CPE parallel connection is given by:

$$Z_{R-CPE} = \frac{R}{1 + RY_0(j\omega)^n}, \tag{3}$$

where Y_0 is the admittance of the CPE and n is the CPE exponent. The n takes the value of 1 when it corresponds to a capacitor, it is between $0.5 < n < 1$ when a non-ideal capacitor behavior occurs, n equals 0.5 when the CPE corresponds to a Warburg impedance describing a diffusion process, and finally, n equals 0 when it represents a resistor [85]. Using the CPE together with the Cole-Cole approach [83,86], the capacitance can be calculated from the fittings by:

$$C = \sqrt[n]{\frac{RY_0}{R^n}}. \tag{4}$$

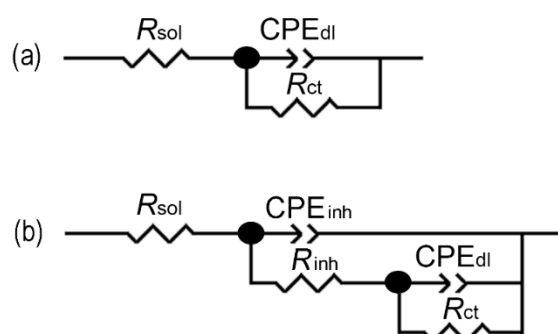


Figure 21. Electrochemical impedance spectroscopy (EIS) equivalent circuits used for numerical simulation of the EIS data obtained for the mild steel panels after submission in the electrolytic solutions in the absence or presence of corrosion inhibitors: (a) equivalent circuit with three elements, (b) equivalent circuit with five elements.

The equivalent circuit for both the untreated mild steel and the systems including MBT (*Steel–WSS–MBT*, *Steel–NaCl–MBT*) after exposure to either WSS or 3.5 wt % NaCl includes three components and corresponds to an EIS spectrum comprising of one time constant. In particular, it consists of the solution resistance (R_{sol}), the charge transfer resistance together with a double-layer CPE (R_{ct} – CPE_{dl}) that are attributed to the presence of corrosion active pits either at the mild steel surface or at the metal–inhibitor interface, as shown in Figure 21a.

Regarding the systems including both Na_2HPO_4 –MBT or only Na_2HPO_4 in either WSS or 3.5 wt % NaCl (*Steel–WSS– Na_2HPO_4* , *Steel–WSS– Na_2HPO_4 –MBT*, *Steel–NaCl– Na_2HPO_4* , *Steel–NaCl– Na_2HPO_4 –MBT*), the relative equivalent circuit consists of five components and corresponds to an EIS spectra of two relaxation times. More specifically, it includes the resistance of the solution (R_{sol}), the pore resistance, and the CPE of the inhibitor layer (R_{inh} – CPE_{inh}) in parallel connection, which are attributed to the response of the electrolyte inside the pores of the layer, and finally, the charge transfer resistance and the double-layer CPE (R_{ct} – CPE_{dl}) that are due to the presence of the corrosion process.

Taking into account the aforementioned Equation (4), the C_{inh} , C_{int} , and C_{dl} parameters were calculated. In principal, the C_{dl} value is influenced by the roughness of the metal surface [38,39]. The determined values of the EIS fitting parameters for the WSS and 3.5 wt % NaCl electrolytic solutions are tabulated in Tables S2 and S3, respectively. However, taking into account the CPE_{inh} -P values [CPE_{inh} -P represents the n which is the CPE exponent in Equations (3) and (4)] calculated for the *Steel–WSS– Na_2HPO_4 –MBT* (0.50334) and *Steel–WSS– Na_2HPO_4* (0.50486) samples after exposure to WSS solution for 96 h, it can be mentioned that these elements cannot be associated to a non-ideal capacitor (Table S2) [84]. Similar assessments can be reported for the CPE_{inh} -P values determined for the *Steel–NaCl– Na_2HPO_4 –MBT* sample after exposure to 3.5 wt % NaCl solution for 24 h (0.5009), 48 h (0.50201), 72 h (0.50471), and 96 h (0.50474), as well as for the *Steel–NaCl– Na_2HPO_4* sample after exposure to 3.5 wt % NaCl solution for 96 h (0.50913) (Table S3). Nevertheless, it should be mentioned that the introduction of a Warburg impedance component did not improve the numerical fitting of the EIS results. Moreover, it should be taken into consideration that Tables S2 and S3 do not demonstrate the mean values of the EIS fitting parameters. Finally, considering the obtained R_p and R_{ct} values of Table 4 and Tables S2 and S3, it can be stated that both LPR and EIS methods confirm that the systems including both Na_2HPO_4 and MBT inhibitors exhibit the best anticorrosive behavior after 96 h of exposure to either WSS or 3.5 wt % NaCl electrolytic solutions.

The evolution of the mean values together with the corresponding error bars of the EIS fitting parameters R_{ct} , C_{dl} of the mild steel panels after their exposure to WSS solution for 96 h in the presence or absence of corrosion inhibitors is depicted in Figure 22. Concerning the determined values, it can be mentioned that the system including both the inhibitors Na_2HPO_4 and MBT exhibits the highest R_{ct} values for all the exposure time intervals. It is important to notice that high R_{ct} values indicate enhanced resistance to the corrosion process [87]. On the other hand, the lowest low C_{dl} values are observed for the

system containing the inhibitors Na_2HPO_4 , revealing a low corrosion reaction area [87]. Furthermore, small variations are discerned in the C_{dl} of this system, indicating that the corrosion reaction area does not undergo changes. Consequently, the inhibitor Na_2HPO_4 either alone or in combination with MBT provides the best protection to mild steel against corrosion in WSS solution (Table S2).

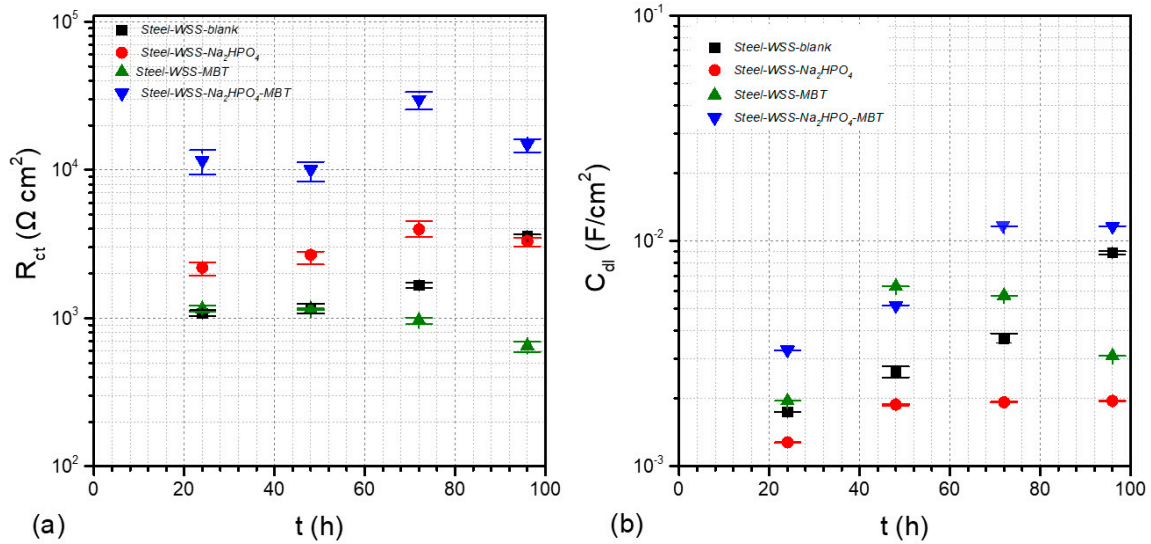


Figure 22. The evolution of the mean values of the EIS fitting parameters as a function of time for mild steel panels after submission in WSS: (a) R_{ct} , (b) C_{dl} .

Analyzing the evolution of the EIS fitting parameters R_{ct} , C_{dl} of the mild steel panels after their subjection in 3.5 wt % NaCl solution for 96 h in the presence or absence of corrosion inhibitors (Figure 23), it can be noticed that that the system including both the inhibitors Na_2HPO_4 and MBT reveals the highest R_{ct} values together with the lowest C_{dl} values for all the exposure time intervals. Therefore, the combination of both inhibitors Na_2HPO_4 and MBT performs the best protection to mild steel against corrosion in 3.5 wt % NaCl solution (Table S3). Furthermore, it appears that all the systems including inhibitors exhibit higher R_{ct} values compared to the *Steel-NaCl-blank*, indicating effective corrosion protection to mild steel.

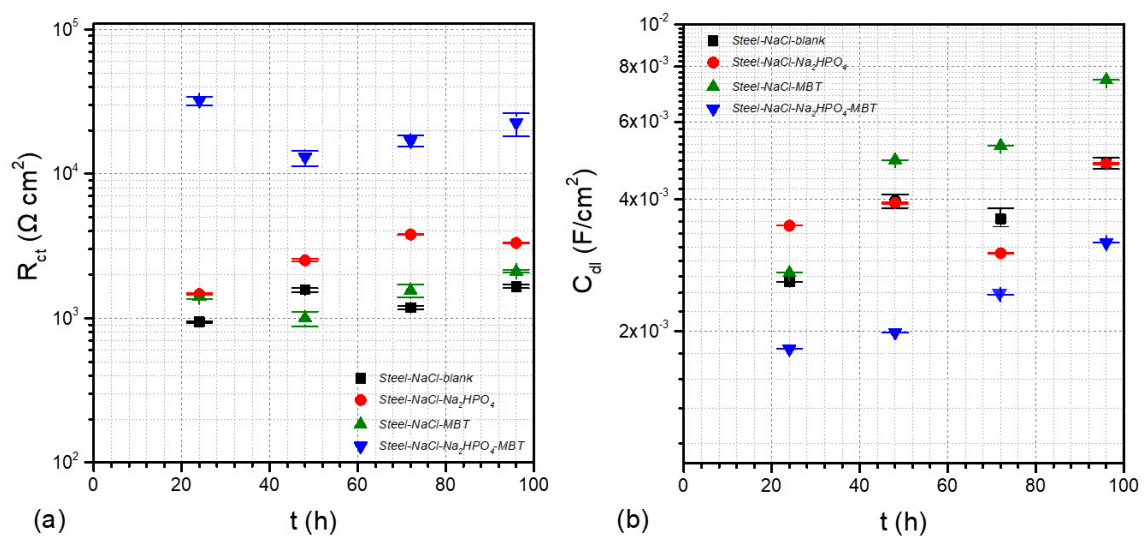


Figure 23. The evolution of the mean values of the EIS fitting parameters as a function of time for mild steel panels after submission in 3.5 wt % NaCl: (a) R_{ct} , (b) C_{dl} .

The tabulated values of $\eta(\%)$ derived from Equation (1) after 24, 48, 72, and 96 h of mild steel samples submission either in WWS solution or into 3.5 wt % NaCl solution, in the presence or absence of inhibitor, are illustrated in Tables S2 and S3, respectively. The results reveal that for all the time intervals, the highest values of $\eta(\%)$ appear for the systems including both inhibitors Na_2HPO_4 and MBT, denoting enhanced corrosion inhibition to mild steel. Furthermore, according to the obtained $\eta(\%)$ values, it may be remarked that the system containing the Na_2HPO_4 provides also improved protection to mild steel against corrosion. Finally, it should be noted that for the *Steel–WSS–MBT* sample, the $\eta(\%)$ values could be calculated for 48, 72, and 96 h since the corresponding R_{ct} values are lower than those of the *Steel–WSS–blank* sample. The same result was revealed for the *Steel–WSS–Na₂HPO₄* sample after 96 h of subsection in WWS solution as well as for the *Steel–NaCl–MBT* after 48 h of exposure to 3.5 wt % NaCl solution. These outcomes clearly denote that the presence of the inhibitor MBT into the WWS solution cannot provide adequate corrosion protection to mild steel after 48 h.

3.5. Corrosion Inhibition Mechanism

Taking into account the aforementioned obtained results, the following corrosion inhibition mechanism can be claimed that is in accordance with the dry–wet–dry model, which is illustrated by the equal model of Evans (differential aeration corrosion cell), considering the four-stage model of Fontana and Greene [77].

3.5.1. The Main Pathway of Corrosion Process in an Fe–C/NaCl_(aq) System

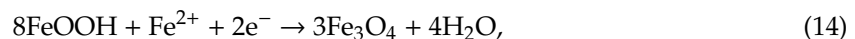
Taking into account the mild steel submission in the saline solution, a milestone for the initiation of corrosion could be considered the time when the first ferrous ions (Fe^{2+}) or ferric ions (Fe^{3+}) ions release (Reactions 5 and 6), defining the anodic site that emerges near the metallic surface. Subsequently, the local charge density increases, causing the appearance of the cathodic current, and taking into account that the pH of the electrolytic solutions was in a range from 7.33 to 7.97, the dissolved O_2 reacts with H_2O and becomes reduced to OH^- ions (Reaction 7). In the same way, as in the case of mild steel, the alloying elements release Mn^{2+} , Cu^{2+} , and other cations, originating from the dissolution of the alloy equally to Fe oxidation and maintaining the stoichiometric ratio they used to have in the alloy. The consequent excess either of Fe^{2+} or Fe^{3+} and OH^- of the main oxidation–reduction reactions (8, 9) results in the precipitation of iron hydroxides from the solution to the corroded surface.



The obtained $\text{Fe}(\text{OH})_2(\text{s})$ and $\text{Fe}(\text{OH})_3(\text{s})$ create a thick gel, either precipitating from the solution or created very close to the metallic surface where oxygen concentration is very low to negligible. This thick gel is characteristic of wet rapid corrosion [88], which represent an appropriate precursor for the first types of iron oxides and oxide–hydroxides. Moreover, the visualization of the primary redox processes arises as an initial thin adherent layer on the steel surface, which is empirically metallic gray or black in color. This inner layer consists mainly of Fe_3O_4 (magnetite) and $\gamma\text{-Fe}_2\text{O}_3$ (maghemite) and/or $\gamma\text{-FeO}(\text{OH})$ (lepidocrocite), insoluble Fe(III) solid phases, as was also commented in spectroscopic measurements. On the other hand, the bulk layer (of the overall electrochemical double layer) consists of (i) oxides from the alloying elements dissolution such as heavy metal oxides, i.e., Mn_2O_7 , (ii) interstitial complex phases, i.e., the known ferrites and ferrates (mixtures chiefly of iron oxides and other metallic oxides) [89], and (iii) various intermediates stemming from oxidation and

corrosion phenomena, local physicochemical conditions (pH, ions concentration etc.) and physical parameters such as the humidity or aeration level of the surface.

Consequently, charge separation takes place and signals the start of the second phase of the corrosion mechanism on a mild steel surface, according to the Evans model perspective. As mentioned, in anodic areas, $\text{Fe}(\text{OH})_2$ and $\text{Fe}(\text{OH})_3$ create a characteristic thick gel that restricts the diffusion of the products of reduction semi-reactions such as O_2 and OH^- , which are usually responsible for the rust layer deterioration at a later stage. Additionally, Cl^- , which originates in the $\text{NaCl}_{(\text{aq})}$ solution and the soluble forming Fe–Cl salts ionization (reactions 10, 11), since they are more reactive than OH^- , they tend to attack the protective layer, reacting with the agile Fe^{2+} of the anodic dissolution, triggering a series of local corrosion phenomena, which would open the way even to reach and hazard the inner layer (reactions 12, 13). For example, in wet conditions, the chemical reactions (5) and (14) occur, indicatively:



After a relative stabilization of the primary oxidation processes and iron oxides and hydroxides interaction, the eventually generated [Fe–O–OH] thick gel, which is chemically attached to the inner layer of corrosion products, obtains a unique for each system constitution of crystalline iron oxide phases. This constitution depends on the Fe^{2+} , Fe^{3+} , and dissolved O_2 , OH^- availability, the mixture of which is responsible for the emergence of a pioneering family of materials, the layered double hydroxides (LDH) [90,91], with green rust as the main representatives in literature [92,93]. Taking into account that the direct oxidation of iron or low-alloyed steel to the unstable ferric ions (Fe^{3+}) is restricted thermodynamically against the generation of ferrous ions (Fe^{2+}), it could be assumed that the concentration of the former would be found to be negligible, referring to the whole rust layer structure.

In particular, the identification of green rusts (LDH structures) in the obtained corrosion products denotes that ferric ion creation is favored. Moreover, as the forming Fe–Cl salts were expected to have been dissolved, and were considered totally soluble in the present aqueous system, the chlorides detection in the rust layer indicates that sulfate green rust structures could have captured chlorides [94–96]. After a relative stabilization of the double layer, with the inner layer to consist mainly of magnetite (Fe_3O_4), mass transfer, electromigration and more time-consuming phenomena take place, depending on the local physicochemical conditions and compounds concentrations. In the mere aqueous saline system of mild steel, it was expected that the Cl^- would attack and damage the magnetite passive film, triggering a series of local corrosion phenomena, as analyzed in the aforementioned paragraph. Hence, as referred also in spectroscopic measurements, Cl^- were not expected to be detected in solid phases, as they are very soluble in the current system [97].

Essentially, the generated Fe^{2+} and e^- from the mild steel dissolution in anode diffuse through the inner layer (or magnetite layer) and provoke the cathodic precipitation of magnetite, reducing the continuously forming oxyhydroxides according to reaction (9) and conferring a particular thickness to the bulk rust layer. In case of aeration or in the presence of a sufficient quantity of dissolved oxygen, for the wet condition, water and oxygen molecules pass through the $\text{FeO}(\text{OH})$ outer layer and oxidize magnetite, forming again stacking oxyhydroxides and interstitial species mainly of [Fe, O, OH], bonding with oxygen bridges and hydrogen bonds in a near-neutral environment (reaction (15)).



A more acceptable approximation for the latter would be the formation of Fe-OH-OH, which is more stable [44]. A significant variable is the surface charge of the outer FeO(OH) layer, depending on the protonation of Fe-OH-OH for a wet near-neutral environment, and deprotonation of the Fe-OH-OH layer in more acidic conditions. In the conventional natural mild steel saline system, the more time-consuming mechanisms and solid-state transformations are considered to proceed evermore, due to the thermodynamic equilibriums of each particular molecular interaction (aging). Characteristic processes of that stage are the further dehydration and crystallization of the oxyhydroxides and of the Fe(OH)₃, as previously observed even in wet conditions, underlying the outer rust layer. Additionally, complicated structures of crystalline flowers, honeycombs, nests, rods, and other unique formations emerge, as described elaborately in our SEM analysis, which were generated axially with regard to the metallic surface, as part of a family of processes that is responsible for illustrating the rust layer constitution for the most of the mild steel corrosion investigations in the past.

3.5.2. Corrosion Inhibitors

According to the literature, two main corrosion inhibition mechanisms for mild steel protection have proved to be more reliable [77]. The first one is through chemisorption onto the mild steel surface, limiting the metal dissolution rate by forming an adherent passive film, as MBT does for lightly acidic and near-neutral aqueous systems [78]. The second one is by the formation of a new phase onto the metallic surface, creating a conversion coating, as during the phosphating process.

Mercapto functional azole compounds present enhanced inhibitive efficiency to mild steel. The coexistence of sulfur and nitrogen atoms in the heterocyclic ring of the inhibitor molecule provides increased binding capability for the inhibitor attachment [98,99]; the aromatic ring of the molecule is known for its contribution to increase electronic density [100], whilst the higher electronegativity of sulfur than that of nitrogen renders the thiol group an especially efficient electron donor [29,99]. Particularly, according to the works of Chen et al. [29] and Obot et al. [101], it can be claimed that of the two tautomers of MBT, thiol (MBT-thiol) or thione (MBT-thione) (Figure 24a), coexisting usually in ionic solutions and ambient temperatures, the second seems to be more stable, especially in solid state, as in rusts. The latter group of researchers mentioned by the means of chemical hardness measurements that MBT-thione has increased electronegativity compared to MBT-thiol, which confers to the former a denser electronic cloud around the functional mercapto group of the molecule, and hence enhanced inhibition ability. Considering that electronegativity is proportionate to the chemisorption of the inhibitor and therefore to the level of its inhibition ability [100], they found that the heterocyclic ring could bond to the metallic surface through the endocyclic nitrogen, as the most electronegative of the three more possible donors. Furthermore, and at the same time, the heterocyclic ring could also bond with the exocyclic sulfur, chelating in that manner the iron cations and attaching, with its planar aromatic ring parallel to the metallic surface.

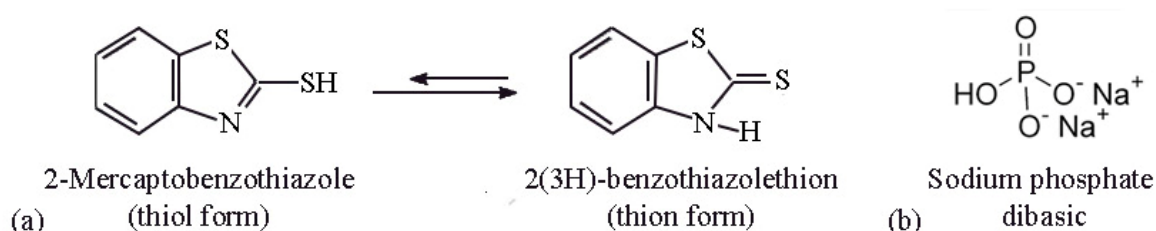


Figure 24. Schematic representation of (a) 2-mercaptobenzothiazole (thiol form) and 2(3H)-benzothiazolethion (thion form); (b) sodium phosphate dibasic [Na₂HPO₄].

In our study, the most electronegative positions would be the two atoms of sulfur. In spite of the electrostatic interaction preference, due to steric hindrance, the more stable coordination geometry of the MBT-thione with mild steel was commented to realize by means of the exocyclic sulfur, with the aromatic plane perpendicular to the metallic surface. The two tautomeric types of MBT usually coexist

in circumneutral aquatic and ionic solutions [102], but be that as it may, a supplementary clue in favor of the thione mode, as predominant in the rust layer, emerges from a characteristic Raman shift in the *Steel-WSS-Na₂HPO₄-MBT* sample.

Taking into account that MBT-thione inhibition efficiency upon time depends on the rate of the attachment of the exocyclic sulfur to mild steel, two stages of the inhibitor adsorption were distinguished [29]. The first stage is meant to be a physisorption process of the organic hydrolyzed molecule to the solid metallic surface, leading to the creation of a primary monomolecular layer. Physical binding of the inhibitor needs relatively low quantities of exchangeable energy, takes place to a limited extent as a front reaction, and is the prominent and necessary process for the inhibitor's attaching and hence to initiate the adsorption of the inhibitor [99]. The second stage, chemisorption, is also quickly initiated, as Fe-S chemical bonding is considered to be prompt and more powerful. The two adsorption processes were identified as similar systems to MBT-thione and iron by Obot et al. in 2018. However, the duration of each stage and even of the whole adsorption process and the enhanced stability and uniformity of the final layer imply that a more complicated process had actualized. It was found that MBT has the tendency to form hydrophobic bonds in neutral aquatic electrolytic solutions [103], followed by a self-assembly ordering with characteristic duration [104]. In case of parallel plane geometry to the metallic surface, hydrophobic-originating complexes create locally hydrophobic complexes as metal islands that combine afterwards to a uniform protective layer. In perpendicular orientation, similar mechanisms with hydrophobic intermolecular connections were suggested [65].

Despite the appearing complexity of the adsorption process of MBT, its kinetics were already specified and recorded in the literature, as also the self-assembly process through which the inhibitor lays the protective layer [29,65]. At a second glance, a precise orientation of the planar organic inhibitor could be similar to that proposed in the study of Venkataramanan et al. on the Ag surface [72]. Due to the increased local electronic density and the negative δ contribution on the thiol edge, in conjunction with a commonly observed attitude of S to alter the planarity of MBT-thione [100,105] and bend the S-C bond [103], it seems as the most probable scenario that the inhibitor attaches onto a mild steel surface, with the exocyclic sulfur-carbon bond perpendicular to metal and the remainder planar molecule angled [65]. In that way, the imminent rearrangement process, which initiates the self-assembly of the protective layer, would lack steric hindrance, as each molecule-plane could be simultaneously strongly chemically bonded onto the metal through an exocyclic sulfur atom. On the other hand, the slightly negatively charged remainder planes would be free to rotate, providing a relevant ionic permeability to the protective layer and diminishing the possibility for the layer rupture.

Phosphorus consists of a significant alloying element of low-alloyed and carbon steels against atmospheric corrosion [106] and Cl⁻ attack [107], and it is considered to improve machinability, fatigue, and hardenability. Phosphating through immersion baths, as conventionally realized in industry, is considered to be complete after several days, mainly due to recrystallization and solid-state transformation processes and in order to enhance surface coherence with metallic coatings, as zinc phosphating [53] and even with organic protective coatings. There has been a variety of chiefly organic substances proposed as accelerators of phosphating, such as certain imines, pyridines, and other oxidizing substances [108]. Phosphate anions have been considered to confer satisfying corrosion resistance, stabilizing both crystalline and amorphous phases in the corrosion product layer [109]. Although inorganic phosphorus-containing compounds were broadly utilized against the corrosion and wear phenomena of mild steel, and its crystallization kinetics and pathways were intricately investigated in ambient conditions [110], there are impenetrable aspects to explore up to date, from the interatomic to hypercrystalline level. Not only does phosphorus bind strongly to common non-metals such as oxygen and nitrogen, it also does so with metals and minerals consisting of oligomeric or near-polymeric complexes, such as ferrates and polyoxometallates. In phosphate tetrahedra, the phosphorus is strongly bonded to oxygen atoms, and their bond length could be found to be even fourfold inside the same solid (bond-stretch isomerism) [59,110]. In particular, inorganic phosphate

tetrahedra (mainly PO_4^{3-} , HPO_4^{2-}) behave as relatively strong Lewis bases, maintain their bonding in aquatic near-neutral solutions, and precipitate forming insoluble salts with the locally available cations (Figure 24b). In ambient conditions, they coordinate in hypercrystalline structures and minerals through tetrahedra or octahedra (or connected trioctahedra by others [111], linking by corners or edge sharing that form chains, clusters, and sheets [112–114].

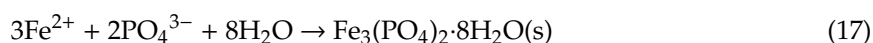
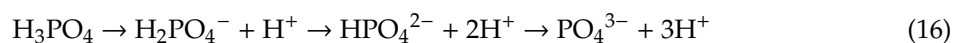
In the aquatic system of our study, equally to the increase in local electronegativity and valence of the cations, phosphates tend to form the most thermodynamically stable hypercrystalline structures, with an ascending affinity to cyclic or/and branched complexes, with the latter to be achieved either through electrostatic attraction to small cations, as Cl^- , SO_4^{2-} , CO_3^{2-} or with ligand exchange, as with solid crystalline phases and metastable iron aqua ions [indicatively FeOH^{2+} , $\text{Fe}(\text{OH})_4^-$, $\text{Fe}(\text{OH})^{2+}$, and $\text{Fe}(\text{H}_2\text{O})_6^{2+}$], which were formed through the hydration, olation, or oxolation of ferrous and ferric species [109,113,115,116]. It is established that transition metals can exchange a mere electron, whereas non-metal reactive species, as dioxygen and radical species, are restricted by Pauli's principle, reacting in a slower way [109]. Specifically, between 5 and 9 pH values, the instantly forming ferric salts hydrolyze immediately, while ferrous salts, in the absence of oxidizing substances, react with water, resulting in aqua ions generation, as $\text{Fe}(\text{H}_2\text{O})_6^{2+}$.

Generally, ferric complexes tend to condense from very acidic (near pH 1, room temperature) up to near neutral solutions, conferring interstitial oligomeric or/and polymeric Fe(III) compounds that are named as ferrihydrites [117], while ferrous complexes condense only above pH 6 and in oxygen deprivation onto the hardly accessible metal surface, where they are hydrolyzed, to precipitate as $\text{Fe}(\text{OH})_2$. A chain of reactions occur in the meanwhile, as the olation of the dimeric $[\text{Fe}_2(\text{OH})_8(\text{H}_2\text{O})_8]^{2+}$ complex to planar tetrameric $[\text{Fe}_4(\text{OH})_8(\text{H}_2\text{O})_8]^0$, and the following rapid nucleation of the mentioned tetrahedral and/or octahedral interstitial formations, simultaneously at many sites of each emerging plane, initiating a process of crystalline epitaxial growth for the generation of the layered double hydroxides. The ferrous phases, either in solution or in solid state, have expressed a propensity to oxidation, from which mixed ferric-ferrous phases are considered to be formed, known as green rust, magnetite, goethite and lepidocrocite. In the literature, two physicochemical pathways for phosphorus bonding are distinguished. A fraction of it is rapidly adsorbed and triggers the conversion process of mild steel surface, whereas most of the phosphorus is gradually diffusing into the crystalline iron oxide and hydroxide compounds of the inner layer, as in case of goethite, either into the pores or into the crystal lattice [118].

It was reported that at pH 7, the transformation of $\text{Fe}(\text{OH})_2$ to lepidocrocite is a characteristic reaction, in conjunction with a noted elevation of the potential [109], whereas the hydrolysis and then the aggregation of ferrihydrites often results in the crystallization of goethite and hematite, which is a process chiefly depending on the oxolation of metastable $[\text{Fe},\text{OH},\text{O}]$ species [107,117,119]. Phosphate anions are considered to have a unique coordination effect in the corrosion process by executing selective adsorption in different phases [21,107]. Ascending to the microscale, phosphates seem to play a binary role in ferrous corrosion products, either by being adsorbed into iron oxides and oxyhydroxides, as into goethite and lepidocrocite crystal lattices, with the creation of bidentate surface complexes by replacing two hydroxyls—their main ion competitor in aquatic solutions [118,120–123]—or by binding on mild steel surface molecules and forming phosphate and iron phosphate crystalline structures, creating new active sites for further phosphorus adsorption [122]. After all, it could be claimed that the dominant structures of the double-layer compounds are those of iron oxides and hydroxides, whereas into the inner layer of mild steel, hybrid crystalline and amorphous combinations of $[\text{Fe},\text{O}_2],\text{H}_2\text{O},\text{HPO}_4^{2-},\text{PO}_4^{3-}]$ compounds are commonly solidified, providing a unique composition and behavior for each layer.

The investigation of ambient aquatic circumneutral systems of corroding mild steel revealed that a variety of crystalline iron–phosphate products were to be detected, interstitial of the different stoichiometry and oxidation states of iron, during the successive alteration of local conditions, from vivianite (ferrous phosphate), $\text{Fe}_3(\text{PO}_4)_2 \cdot 8\text{H}_2\text{O}$, to strengite (ferric), $\text{FePO}_4 \cdot 8\text{H}_2\text{O}$ (reactions 16,

17) [74,124,125]. The final constitution of the converted coating is meant to emerge by the balancing of the competitive processes of ionic precipitation, solid-state transformations, and crystallization, in conjunction with the local reagent concentrations and aeration level. In accordance with the experimental results, we assume that phosphate anions converted successfully onto the steel surface, participating in green rust stabilization, preventing GRI(Cl^-) oxidation [107] and fine-grained crystalline well-ordered structures in the final rust layer.



3.5.3. The Synergistic Effect

Table 5 presents the calculated values of the synergistic parameter (S_i) using Equation (2). In general, the synergistic effect can be described as the trend, whereas the combination of two or more compounds results in greater action than of those of the individual compounds. Regarding the corrosion inhibition, the synergistic effect refers to the effective interaction of two or more substances in respect of the protection of a material against corrosion.

Table 5. Tabulated values of the synergistic parameter (S_i) calculated using Equation (2).

	Time of Exposure (h)	Synergistic Parameter (S_i)
<i>Steel-WSS-Na₂HPO₄-MBT</i>	24	4.76
<i>Steel-NaCl-Na₂HPO₄-MBT</i>	24	22.6
<i>Steel-WSS-Na₂HPO₄-MBT</i>	96	1.99
<i>Steel-NaCl-Na₂HPO₄-MBT</i>	96	4.22

The synergistic effect can be considered as an effective method to enhance the inhibitive properties of a compound corrosive media. A value of (S_i) > 1 indicates the existence of inhibition synergism between the two compounds, whereas (S_i) = 1 means that no interaction between the two compounds exists; when (S_i) < 1, it denotes toward an antagonistic effect. The synergistic effect of the corrosion inhibition behavior of MBT and Na_2HPO_4 in a molar ratio of 1:1 revealed that the admixture performed effectively with an inhibition efficiency above 90%, R_{ct} up to 6.7 kohm cm^2 and with a synergistic parameter above 22. The synergistic effect of the corrosion inhibition behavior of MBT and Na_2HPO_4 is increased in the presence of NaCl due to the Cl^- interaction. In synergism with the organic inhibitor, phosphate was capable of converting appropriately the corroding surface and in parallel to enhancing the local positive electronic cloud, above the inner layer, encountering the negative abundance of the organic voluminous inhibitor, accelerating and boosting in that way the corrosion inhibitive action of both substances. By the means of electrochemical, spectroscopic, microscopic, and image analyzing techniques of characterization, it is excluded that the acceleration and enhancement of the highly efficient Na_2HPO_4 inhibition was achieved, in combination with the mitigation of the disadvantages of MBT, especially in near-neutral aquatic solutions of mild and low-alloyed steel. The synergistic effect resulted in the formation of more compact and more durable film, which significantly retards the corrosion process.

Surface hardening was achieved as well as a considerable increase in the coherence of corrosion product layer, by developing microstructures with ameliorated resistance against the wear effects of mild steel at the micro and nanoscale, originating from fine-grained phases with powerful bonding not only inside the various chemical species but also between them [124]. Achieving the creation of α -crystals, as goethite and hematite, and the prolonged protection of the converted magnetite layer, it seems reasonable that we have the most thermodynamically stable phases due to the face-centered cubic (fcc) and hexagonal close-packed (hcp) systems, which are the crystalline structures with the highest density, and due to their connectivity provided by phosphorus [126]. The unique chemical

connection of the phosphated mild steel surface, by means of the electronegative, non-polar –SH edge of the organic planar part of the layer, is able to rotate, conferring to the bonding flexibility, as it facilitates ions mobility, which confers the most powerful chemical bonding to the metal (Figure 25). The complex interacts with the outer iron oxides and hydroxides, thus maintaining relatively electrical surface neutrality. Moreover, it was intervened not only in interatomic but also in intermolecular interactions, with the final layer to have significantly increased resistance to corrosive factors, encountering both mass transfer and electrochemical attacking phenomena. The rust layer's outer surface is considered to have a chemical composition consisting of green rusts, $\text{FeO}(\text{OH})$, and Fe_xO compounds, binding with hydrogen bonds and oxygen bridges; therefore, the point of zero charge of them fluctuates, especially for the α -crystals, between iron oxides and oxyhydroxides, from 7.5 to 9.38 at 22 °C. That confers to the layer to have a dynamic response to the increase of the pH locally, for a specific quantity i.e., of a basic compound and to function as an ion trap for the metallic surface [111,124,127].

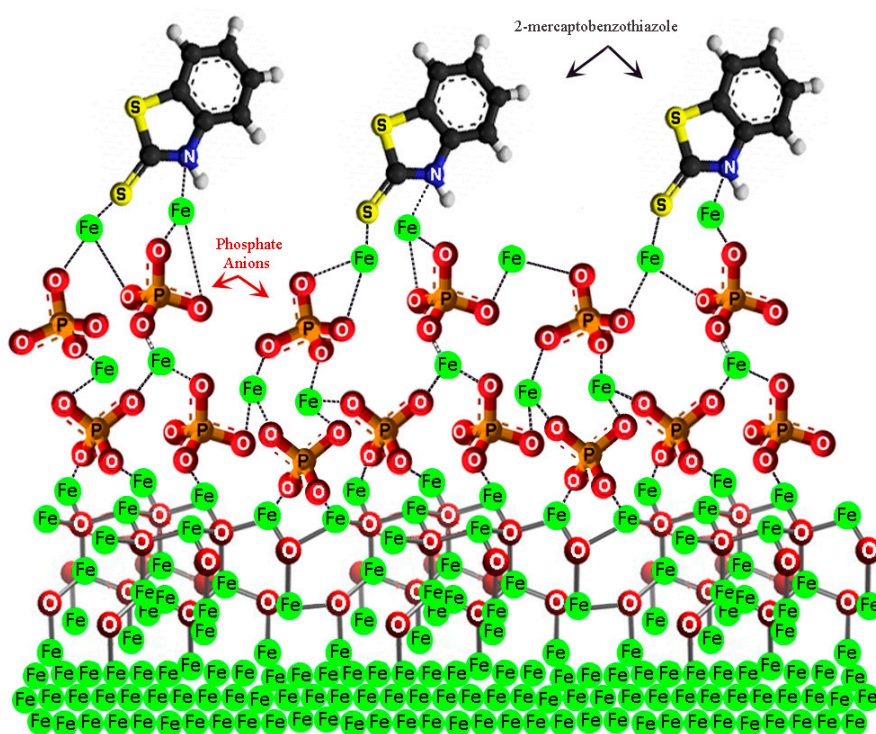


Figure 25. Schematic representation of the phosphate anions and MBT connections onto the mild steel surface, resulting in the formation of the protective film.

4. Conclusions

The electrochemical characterizations demonstrated that MBT and Na_2HPO_4 can be considered as corrosion inhibitors of steel. The initial mixture of corrosion products constitutes a primary viscous layer on the mild steel surface, which afterwards undergoes gradation and is separated into two distinguishable layers: an adherent rust layer and a loosely adherent anodic oxide film. At an early stage, amorphous masses of oxides with spongy appearance are created that transform chiefly to lepidocrocite, part of which is further transformed in goethite. During submission, the reduction of lepidocrocite to hydrated Fe^{2+} intermediate takes place due to metal anodic dissolution, especially near the steel surface, where magnetite appears. The chloride ions are considered to accelerate the corrosion process as aggressive anions, penetrating the protective layer and hence attacking the fresh unharmed metal surface beneath the layer, triggering pitting corrosion.

Adsorbed phosphate is assumed to act as a precursor for hematite creation and often for goethite nucleation and growth; at different concentrations and especially at locally more basic areas, phosphate

anions increase the negative electronic charge of ferrihydrite (present at earlier stages) between particles, and therefore, the formation of hematite retards or is limited. The interaction of ions or neutral molecules at the electrical double layer changes its properties and structures. The water molecules pre-adsorbed at the metal surface in contact with the aqueous solution are involved in the successive adsorption processes. A thin multimolecular adsorption layer via the self-assembly process was formed (phosphonate layer formation) due to the intermolecular interaction between phosphonate groups. The inhibition mechanism is anodic type, hindering the active iron dissolution to a large extent.

Since MBT contains polar groups with an atom of nitrogen and sulfur, the inhibiting properties were determined by the electron density at the reaction center. With an increase in the electron density at the reaction center, the chemisorption bonds between the MBT and the metal are strengthened. Therefore, MBT is adsorbed on the surface of mild steel, forming stable produced self-assembled monolayers of MBT compounds on the surface of mild steel, protecting from aggressive ions. The inhibitive action of MBT takes place through the adsorption of its molecules onto the mild steel surface via the lone pair of electrons of the N and S atoms. The presence of both aforementioned inhibitors into the corrosive environment exhibited the highest impedance modulus and R_{ct} value as the exposure time elapsed. The synergistic effect of the corrosion inhibition behavior of MBT and Na_2HPO_4 in a molar ratio of 1:1 revealed that the admixture performed effectively with inhibition efficiency above 90% and with a synergistic parameter above 22. The synergistic effect of the corrosion inhibition behavior of MBT and Na_2HPO_4 is increased in the presence of NaCl due to the Cl^- interaction. Considering the electrochemical, spectroscopy, and morphology characterizations, the corrosion protection mechanisms of steel can be attributed to the protective layers formed onto the metal surface due to the presence of the inhibitors, which prevent chloride's penetration.

Supplementary Materials: The following are available online at <http://www.mdpi.com/2076-3417/10/1/290/s1>, Table S1. Classification of the Raman spectra peaks. Table S2. Fitting parameters according to equivalent circuits of Figure 21 obtained for the mild steel immersed in WSS solution. Table S3. Fitting parameters according to equivalent circuits of Figure 21 obtained for the mild steel immersed 3.5 wt % NaCl solution.

Author Contributions: I.A.K., P.S., and C.A.C. conceived and designed the experiments. P.S. and I.A.K. conducted the experiments. I.A.K., P.S., and E.K.K. performed the characterization and evaluation of the data. I.A.K., P.S., and C.A.C. discussed the data and wrote the paper. All authors have read and agreed to the published version of the manuscript.

Funding: This research received no external funding.

Conflicts of Interest: The authors declare no conflict of interest.

References

1. Evans, U.R.; Taylor, C.A.J. Mechanism of atmospheric rusting. *Corros. Sci.* **1972**, *12*, 227–246. [[CrossRef](#)]
2. Smith William, F.; Hashemi, J.; Wang, S.-H. *Foundations of Materials Science and Engineering*, 4th ed.; McGraw Hill: New York, NY, USA, 2006.
3. Raman, A.; Nasrazadani, S.; Sharma, L. Morphology of rust phases formed on weathering steels in various laboratory corrosion tests. *Metallography* **1989**, *22*, 79–96. [[CrossRef](#)]
4. Chen, Y.Y.; Tzeng, H.J.; Wei, L.I.; Wang, L.H.; Oung, J.C.; Shih, H.C. Corrosion resistance and mechanical properties of low-alloy steels under atmospheric conditions. *Corros. Sci.* **2005**, *47*, 1001–1021. [[CrossRef](#)]
5. Malaibari, Z.; Kahraman, R.; Saricimen, H.; Quddus, A. Investigation of atmospheric corrosion of mild steel after treatment by several inhibitor solutions. *Corros. Eng. Sci. Technol.* **2013**, *42*, 112–118. [[CrossRef](#)]
6. De la Fuente, D.; Díaz, I.; Simancas, J.; Chico, B.; Morcillo, M. Long-term atmospheric corrosion of mild steel. *Corros. Sci.* **2011**, *53*, 604–617. [[CrossRef](#)]
7. Allam, I.M.; Arlow, J.S.; Saricimen, H. Initial stages of atmospheric corrosion of steel in the Arabian Gulf. *Corros. Sci.* **1991**, *32*, 417–432. [[CrossRef](#)]
8. Kamimura, T.; Hara, S.; Miyuki, H.; Yamashita, M.; Uchida, H. Composition and protective ability of rust layer formed on weathering steel exposed to various environments. *Corros. Sci.* **2006**, *48*, 2799–2812. [[CrossRef](#)]

9. Morcillo, M.; Chico, B.; Díaz, I.; Cano, H.; de la Fuente, D. Atmospheric corrosion data of weathering steels. A review. *Corros. Sci.* **2013**, *77*, 6–24. [[CrossRef](#)]
10. Kolotyrkin, Y.M. Third International Congress on Metallic Corrosion. *Br. Corros. J.* **2013**, *1*, 89. [[CrossRef](#)]
11. Siddique, M.; Anwar-ul-Islam, M.; Butt, N.M.; Hussain, N.; Rehman, S.; Arshed, M. Mössbauer study of corrosion of mild steel induced by acid rain. *J. Radioanal. Nucl. Chem.* **1999**, *241*, 239–240. [[CrossRef](#)]
12. Migneault, S.; Koubaa, A.; Perré, P.; Riedl, B. Effects of wood fiber surface chemistry on strength of wood–plastic composites. *Appl. Surf. Sci.* **2015**, *343*, 11–18. [[CrossRef](#)]
13. McCafferty, E. *Surface Chemistry of Aqueous Corrosion Processes*; Springer: New York, NY, USA, 2015. [[CrossRef](#)]
14. Sha, W. *Steels: From Materials Science to Structural Engineering*; Springer: London, UK, 2013. [[CrossRef](#)]
15. Refait, P.; Génin, J.M.R. The transformation of chloride-containing green rust one into sulphated green rust two by oxidation in mixed Cl^- and SO_4^{2-} aqueous media. *Corros. Sci.* **1994**, *36*, 55–65. [[CrossRef](#)]
16. Parkins, R.N. The intergranular corrosion and stress corrosion cracking of mild steel in clarke’s solution. *Corros. Sci.* **1994**, *36*, 2097–2110. [[CrossRef](#)]
17. Mobin, M.; Malik, A.U.; Andijani, I.N. The effect of heavy metal ions on the localized corrosion behavior of steels. *Desalination* **2007**, *217*, 233–241. [[CrossRef](#)]
18. Brinis, H.; Samar, M.E.H. A method for inhibiting scale formation and corrosion in a cooling water system. *Desalin. Water Treat.* **2013**, *52*, 2609–2619. [[CrossRef](#)]
19. Song, F.M. Predicting the mechanisms and crack growth rates of pipelines undergoing stress corrosion cracking at high pH. *Corros. Sci.* **2009**, *51*, 2657–2674. [[CrossRef](#)]
20. Eliyan, F.F.; Kish, J.R.; Alfantazi, A. Corrosion of New-Generation Steel in Outer Oil Pipeline Environments. *J. Mater. Eng. Perform.* **2016**, *26*, 214–220. [[CrossRef](#)]
21. Reeves, N.J.; Mann, S. Influence of inorganic and organic additives on the tailored synthesis of iron oxides. *J. Chem. Soc. Faraday Trans.* **1991**, *87*, 3875. [[CrossRef](#)]
22. Bockris, J.O.M.; Conway, B.E. Hydrogen Overpotential and the Partial Inhibition of the Corrosion of Iron. *J. Phys. Colloid Chem.* **1949**, *53*, 527–539. [[CrossRef](#)]
23. El Ibrahim, B.; Jmiai, A.; Bazzi, L.; El Issami, S. Amino acids and their derivatives as corrosion inhibitors for metals and alloys. *Arab. J. Chem.* **2017**. [[CrossRef](#)]
24. McCafferty, E. *Introduction to Corrosion Science*; Springer Science: Washington, DC, USA, 2010. [[CrossRef](#)]
25. Sanyal, B. Organic compounds as corrosion inhibitors in different environments—A review. *Prog. Org. Coat.* **1981**, *9*, 165–236. [[CrossRef](#)]
26. Refaey, S.A.M.; Abd El-Rehim, S.S.; Taha, F.; Saleh, M.B.; Ahmed, R.A. Inhibition of chloride localized corrosion of mild steel by PO_4^{3-} , CrO_4^{2-} , MoO_4^{2-} , and NO_2^- anions. *Appl. Surf. Sci.* **2000**, *158*, 190–196. [[CrossRef](#)]
27. Marczevska-Boczkowska, K.; Kosmulski, M. 2-Mercaptobenzothiazole as a Corrosion Inhibitor in Low Temperature Ionic Liquids. In *Trends in Colloid and Interface Science XXIV*; Springer: Berlin/Heidelberg, Germany, 2011. [[CrossRef](#)]
28. Goudarzi, N.; Farahani, H. Investigation on 2-mercaptobenzothiazole behavior as corrosion inhibitor for 316-stainless steel in acidic media. *Anti Corros. Methods Mater.* **2013**, *61*, 20–26. [[CrossRef](#)]
29. Feng, Y.; Chen, S.; Zhang, H.; Li, P.; Wu, L.; Guo, W. Characterization of iron surface modified by 2-mercaptobenzothiazole self-assembled monolayers. *Appl. Surf. Sci.* **2006**, *253*, 2812–2819. [[CrossRef](#)]
30. Finšgar, M.; Jackson, J. Application of corrosion inhibitors for steels in acidic media for the oil and gas industry: A review. *Corros. Sci.* **2014**, *86*, 17–41. [[CrossRef](#)]
31. Gunasekaran, G.; Natarajan, R.; Muralidharan, V.S.; Palaniswamy, N.; Appa Rao, B.V. Inhibition by phosphonic acids—An overview. *Anti Corros. Methods Mater.* **1997**, *44*, 248–259. [[CrossRef](#)]
32. *Multicylinder Test Sequences for Evaluating Automotive Engine Oils: Sequence IID*; Sponsored by ASTM Committee B.01 on Automotive Lubricants and D-2 on Petroleum Products and Lubricants; American Society for Testing and Materials: West Conshohocken, PA, USA, 1993.
33. Heit, A.H.; Calvin, C. Corrosion Inhibition Compositions. U.S. Patent C 3, 291 C, 11 September 1962.
34. ASTM A568/A568M-09. *Standard Specification for Sheet, Carbon, Structural, and High-Strength, Low-Alloy, Hot-Rolled and Cold-Rolled, General Requirements for*; ASTM International: West Conshohocken, PA, USA, 2009. [[CrossRef](#)]
35. ASTM D6386-99. *Standard Practice for Preparation of Zinc (Hot-Dip Galvanized) Coated Iron and Steel Product and Hardware Surfaces for Painting*; ASTM International: West Conshohocken, PA, USA, 1999. [[CrossRef](#)]

36. Matsushima, I. Carbon Steel—Atmospheric Corrosion. In *Corrosion Handbook*; Revie, R.W., Ed.; John Wiley & Sons, Inc.: Hoboken, NJ, USA; Etobicoke, ON, Canada, 2008; pp. 515–528.
37. Kelly, R.G.; Scully, J.R.; Shoesmith, D.W.; Buchheit, R.G. The Polarization Resistance Method for Determination of Instantaneous Corrosion Rates. In *Electrochemical Techniques in Corrosion Science and Engineering*; Schweitzer, P.A., Ed.; Marcel Dekker, Inc.: New York, NY, USA, 2002; pp. 125–150.
38. Luo, X.; Ci, C.; Li, J.; Lin, K.; Du, S.; Zhang, H.; Li, X.; Cheng, Y.F.; Zang, J.; Liu, Y. 4-aminoazobenzene modified natural glucomannan as a green eco-friendly inhibitor for the mild steel in 0.5 M HCl solution. *Corros. Sci.* **2019**, *151*, 132–142. [[CrossRef](#)]
39. Fernandes, C.M.; Ferreira Fagundes, T.D.S.; Escarpini dos Santos, N.; Shewry de, M.; Rocha, T.; Garrett, R.; Borges, R.M.; Muricy, G.; Valverde, A.L.; Ponzio, E.A. *Ircinia strobilina* crude extract as corrosion inhibitor for mild steel in acid medium. *Electrochim. Acta* **2019**, *312*, 137–148. [[CrossRef](#)]
40. ASTM G44-99. *Standard Practice for Exposure of Metals and Alloys by Alternate Immersion in Neutral 3.5% Sodium Chloride Solution*; ASTM International: West Conshohocken, PA, USA, 2013. [[CrossRef](#)]
41. Migahed, M.A.; Al-Sabagh, A.M.; Khamis, E.A.; Zaki, E.G. Quantum chemical calculations, synthesis and corrosion inhibition efficiency of ethoxylated-[2-(2-[2-(2-benzenesulfonylamino-ethylamino)-ethylamino]-ethylamino)-ethylamino]-ethyl]-4-alkyl-benzenesulfonamide on API X65 steel surface under H2S environment. *J. Mol. Liq.* **2015**, *212*, 360–371. [[CrossRef](#)]
42. Zhu, Y.; Free, M.L.; Yi, G. Electrochemical measurement, modeling, and prediction of corrosion inhibition efficiency of ternary mixtures of homologous surfactants in salt solution. *Corros. Sci.* **2015**, *98*, 417–429. [[CrossRef](#)]
43. Aramaki, K.; Hackerman, N. Inhibition Mechanism of Medium-Sized Polymethyleneimine. *J. Electrochem. Soc.* **1969**, *116*, 568. [[CrossRef](#)]
44. Tamura, H. The role of rusts in corrosion and corrosion protection of iron and steel. *Corros. Sci.* **2008**, *50*, 1872–1883. [[CrossRef](#)]
45. Revie, R.W. (Ed.) *Uhlig's Corrosion Handbook*; John Wiley & Sons: Hoboken, NJ, USA, 2011. [[CrossRef](#)]
46. Alcántara, J.; Chico, B.; Simancas, J.; Díaz, I.; de la Fuente, D.; Morcillo, M. An attempt to classify the morphologies presented by different rust phases formed during the exposure of carbon steel to marine atmospheres. *Mater. Charact.* **2016**, *118*, 65–78. [[CrossRef](#)]
47. Ma, Y.; Li, Y.; Wang, F. The effect of β -FeOOH on the corrosion behavior of low carbon steel exposed in tropic marine environment. *Mater. Chem. Phys.* **2008**, *112*, 844–852. [[CrossRef](#)]
48. Misawa, T.; Hashimoto, K.; Shimodaira, S. The mechanism of formation of iron oxide and oxyhydroxides in aqueous solutions at room temperature. *Corros. Sci.* **1974**, *14*, 131–149. [[CrossRef](#)]
49. De la Fuente, D.; Díaz, I.; Alcántara, J.; Chico, B.; Simancas, J.; Llorente, I.; García-Delgado, A.; Jiménez, J.A.; Adeva, P.; Morcillo, M. Corrosion mechanisms of mild steel in chloride-rich atmospheres. *Mater. Corros.* **2016**, *67*, 227–238. [[CrossRef](#)]
50. Evans, U.R. Mechanism of rusting. *Corros. Sci.* **1969**, *9*, 813–821. [[CrossRef](#)]
51. Stratmann, M.; Bohnenkamp, K.; Engell, H.J. An electrochemical study of phase-transitions in rust layers. *Corros. Sci.* **1983**, *23*, 969–985. [[CrossRef](#)]
52. Mathew, V.; Kim, S.; Kang, J.; Gim, J.; Song, J.; Baboo, J.P.; Park, W.; Ahn, D.; Han, J.; Gu, L.; et al. Amorphous iron phosphate: Potential host for various charge carrier ions. *NPG Asia Mater.* **2014**, *6*, e138. [[CrossRef](#)]
53. Tiwari, A.; Hihara, L.; Rawlins, J. (Eds.) *Intelligent Coatings for Corrosion Control*; Butterworth-Heinemann: Oxford, UK, 2015. [[CrossRef](#)]
54. Cornell, R.M.; Schwertmann, U. *The Iron Oxides: Structure, Properties, Reactions, Occurrences and Uses*, 2nd ed.; Wiley-VCH Verlag GmbH & Co. KGaA: Weinheim, Germany, 2003.
55. Farzarian, K.; Pimenta Teixeira, K.; Perdigão Rocha, I.; De Sa Carneiro, L.; Ghahremaninezhad, A. The mechanical strength, degree of hydration, and electrical resistivity of cement pastes modified with superabsorbent polymers. *Constr. Build. Mater.* **2016**, *109*, 156–165. [[CrossRef](#)]
56. Gálvez, N. Effect of Phosphate on the Crystallization of Hematite, Goethite, and Lepidocrocite from Ferrihydrite. *Clays Clay Miner.* **1999**, *47*, 304–311. [[CrossRef](#)]
57. Schwertmann, U. Effect of pH on the Formation of Goethite and Hematite from Ferrihydrite. *Clays Clay Miner.* **1983**, *31*, 277–284. [[CrossRef](#)]
58. Antunes, R.A.; Costa, I.; Faria, D.L.A.D. Characterization of corrosion products formed on steels in the first months of atmospheric exposure. *Mater. Res.* **2003**, *6*, 403–408. [[CrossRef](#)]

59. Labinger, J.A. Bond-stretch isomerism: A case study of a quiet controversy. *C. R. Chim.* **2002**, *5*, 235–244. [[CrossRef](#)]
60. Tamilselvi, M.; Kamaraj, P.; Arthanareeswari, M.; Devikala, S.; Selvi, J.A. Development of nano SiO₂ incorporated nano zinc phosphate coatings on mild steel. *Appl. Surf. Sci.* **2015**, *332*, 12–21. [[CrossRef](#)]
61. Dwivedi, D.; Lepková, K.; Becker, T. Carbon steel corrosion: A review of key surface properties and characterization methods. *RSC Adv.* **2017**, *7*, 4580–4610. [[CrossRef](#)]
62. De la Fuente, D.; Alcántara, J.; Chico, B.; Díaz, I.; Jiménez, J.A.; Morcillo, M. Characterisation of rust surfaces formed on mild steel exposed to marine atmospheres using XRD and SEM/Micro-Raman techniques. *Corros. Sci.* **2016**, *110*, 253–264. [[CrossRef](#)]
63. Simard, S.; Odziemkowski, M.; Irish, D.E.; Brossard, L.; Ménard, H. In situ micro-Raman spectroscopy to investigate pitting corrosion product of 1024 mild steel in phosphate and bicarbonate solutions containing chloride and sulfate ions. *J. Appl. Electrochem.* **2001**, *31*, 913–920. [[CrossRef](#)]
64. Dhaiveegan, P.; Elangovan, N.; Nishimura, T.; Rajendran, N. Weathering Steel in Industrial-Marine-Urban Environment: Field Study. *Mater. Trans.* **2016**, *57*, 148–155. [[CrossRef](#)]
65. Sandhyarani, N.; Skanth, G.; Berchmans, S.; Yegnaraman, V.V.; Pradeep, T. A Combined Surface-Enhanced Raman-X-ray Photoelectron Spectroscopic Study of 2-mercaptobenzothiazole Monolayers on Polycrystalline Au and Ag Films. *J. Colloid Interface Sci.* **1999**, *209*, 154–161. [[CrossRef](#)]
66. Socrates, G. *Infrared and Raman Characteristic Group Frequencies*, 3rd ed.; John Wiley & Sons Ltd.: Chichester, UK, 2001; pp. 283–327.
67. De Faria, D.L.A.; Venâncio Silva, S.; de Oliveira, M.T. Raman microspectroscopy of some iron oxides and oxyhydroxides. *J. Raman Spectrosc.* **1997**, *28*, 873–878. [[CrossRef](#)]
68. Kolitsch, U.; Bernhardt, H.-J.; Lengauer, C.L.; Blass, G.; Tillmanns, E. Allanpringite, Fe₃(PO₄)₂(OH)₃5H₂O, a new ferric iron phosphate from Germany, and its close relation to wavellite. *Eur. J. Mineral.* **2006**, *18*, 793–801. [[CrossRef](#)]
69. Zhang, L.; Brow, R.K. A Raman Study of Iron-Phosphate Crystalline Compounds and Glasses. *J. Am. Ceram. Soc.* **2011**, *94*, 3123–3130. [[CrossRef](#)]
70. Liu, Q.; Chen, M.; Zheng, K.; Yang, Y.; Feng, X.; Li, H. In Situ Electrochemical Investigation of Pyrite Assisted Leaching of Chalcopyrite. *J. Electrochem. Soc.* **2018**, *165*, H813–H819. [[CrossRef](#)]
71. Weber, I.; Böttger, U.; Pavlov, S.G.; Hübers, H.W.; Hiesinger, H.; Jessberger, E.K. Laser alteration on iron sulfides under various environmental conditions. *J. Raman Spectrosc.* **2017**, *48*, 1509–1517. [[CrossRef](#)]
72. Venkataramanan, M.; Skanth, G.; Bandyopadhyay, K.; Vijayamohan, K.; Pradeep, T. Self-assembled Monolayers of Two Aromatic Disulfides and a Diselenide on Polycrystalline Silver Films: An Investigation by SERS and XPS. *J. Colloid Interface Sci.* **1999**, *212*, 553–561. [[CrossRef](#)]
73. Ali Asaad, M.; Sarbini, N.N.; Sulaiman, A.; Ismail, M.; Huseien, G.F.; Abdul Majid, Z.; Bothi Raja, P. Improved corrosion resistance of mild steel against acid activation: Impact of novel *Elaeis guineensis* and silver nanoparticles. *J. Ind. Eng. Chem.* **2018**, *63*, 139–148. [[CrossRef](#)]
74. McGowan, G.; Prangnell, J. The significance of vivianite in archaeological settings. *Geoarchaeology* **2006**, *21*, 93–111. [[CrossRef](#)]
75. Morozov, Y.; Calado, L.M.; Shakoob, R.A.; Raj, R.; Kahraman, R.; Taryba, M.G.; Montemor, M.F. Epoxy coatings modified with a new cerium phosphate inhibitor for smart corrosion protection of steel. *Corros. Sci.* **2019**, *159*, 108128. [[CrossRef](#)]
76. Singh, I.; Banerjee, T. Effect of 2-mercaptobenzothiazole on acid dissolution and hydrogen absorption of steel. *Corros. Sci.* **1972**, *12*, 503–515. [[CrossRef](#)]
77. Kelly, R.G.; Scully, J.R.; Shoosmith, D.W.; Buchheit, R.G. Passivity and localised corrosion. In *Electrochemical Techniques in Corrosion Science and Engineering*; Schweitzer, P.A., Ed.; Marcel Dekker Inc.: New York, NY, USA, 2002; pp. 55–124. [[CrossRef](#)]
78. Jafari, H.; Akbarzade, K.; Danaee, I. Corrosion inhibition of carbon steel immersed in a 1M HCl solution using benzothiazole derivatives. *Arab. J. Chem.* **2019**. [[CrossRef](#)]
79. Kasai, N.; Utatsu, K.; Park, S.; Kitsukawa, S.; Sekine, K. Correlation between corrosion rate and AE signal in an acidic environment for mild steel. *Corros. Sci.* **2009**, *51*, 1679–1684. [[CrossRef](#)]
80. Kelly, R.G. Electrochemical thermodynamics and kinetics of relevance to corrosion. In *Electrochemical Techniques in Corrosion Science and Engineering*; Schweitzer, P.A., Ed.; Marcel Dekker, Inc.: New York, NY, USA, 2002; pp. 9–54.

81. Matsushima, I. Carbon Steel—Corrosion in Fresh Waters. In *Corrosion Handbook*; Revie, R.W., Ed.; John Wiley & Sons, Inc.: Hoboken, NJ, USA; Etobicoke, ON, Canada, 2008; pp. 529–544.
82. Matsushima, I. Carbon Steel—Corrosion by Seawater. In *Corrosion Handbook*; Revie, R.W., Ed.; John Wiley & Sons, Inc.: Hoboken, NJ, USA; Etobicoke, ON, Canada, 2008; pp. 545–553.
83. Shifler, D.A.; Aylor, D.M. Testing in environments-seawater. In *Corrosion Tests and Standards Application and Interpretation*; Baboian, R., Ed.; ASTM International: Baltimore, MD, USA, 2005; pp. 362–379.
84. Hsu, C.H.; Mansfeld, F. Technical Note: Concerning the Conversion of the Constant Phase Element Parameter Y_0 into a Capacitance. *Corrosion* **2001**, *57*, 747–748. [[CrossRef](#)]
85. Kong, G.; Lingyan, L.; Lu, J.; Che, C.; Zhong, Z. Corrosion behavior of lanthanum-based conversion coating modified with citric acid on hot dip galvanized steel in aerated 1M NaCl solution. *Corros. Sci.* **2011**, *53*, 1621–1626. [[CrossRef](#)]
86. Cole, K.S.; Cole, R.H. Dispersion and Absorption in Dielectrics II. Direct Current Characteristics. *J. Chem. Phys.* **1942**, *10*, 98–105. [[CrossRef](#)]
87. Shen, S.; Zuo, Y.; Zhao, X. The effects of 8-hydroxyquinoline on corrosion performance of a Mg-rich coating on AZ91D magnesium alloy. *Corros. Sci.* **2013**, *76*, 275–283. [[CrossRef](#)]
88. Kaesche, H. *Corrosion of Metals: Physicochemical Principles and Current Problems*; Springer: Berlin, Germany, 2003. [[CrossRef](#)]
89. Sharma, V.K. *Ferrites and Ferrates: Chemistry and Applications in Sustainable Energy and Environmental Remediation*; American Chemical Society: Washington, DC, USA, 2016; pp. 489–491.
90. Evans, D.G.; Slade, R.C.T. Structural Aspects of Layered Double Hydroxides. In *Layered Double Hydroxides*; Springer: Berlin/Heidelberg, Germany, 2005. [[CrossRef](#)]
91. K. Karaxi, E.; Kartsonakis, I.A.; Charitidis, C.A. Chloride ion entrapment by calcined layered double hydroxides. *Int. J. Struct. Integr.* **2016**, *7*, 788–806. [[CrossRef](#)]
92. Trolard, F.; Bourrié, G. Chapter 5 Geochemistry of Green Rusts and Fougérite. *Adv. Agron.* **2008**, *99*, 227–288. [[CrossRef](#)]
93. Davesne, E.; Dideriksen, K.; Christiansen, B.C.; Sonne, M.; Ayala-Luis, K.B.; Koch, C.B.; Hansen, H.C.B.; Stipp, S.L.S. Free energy of formation for green rust sodium sulphate (NaFeII6FeIII3(OH)18(SO4)2(s)). *Geochim. Cosmochim. Acta* **2010**, *74*, 6451–6467. [[CrossRef](#)]
94. Duan, X.; Evans, D.G. *Layered Double Hydroxides*; Springer: Berlin/Heidelberg, Germany, 2006; Volume 119. [[CrossRef](#)]
95. Li, Y.-H.; Tsui, T.-F. The solubility of CO₂ in water and sea water. *J. Geophys. Res.* **1971**, *76*, 4203–4207. [[CrossRef](#)]
96. Refait, P.; Drissi, S.H.; Pytkiewicz, J.; Génin, J.M.R. The anionic species competition in iron aqueous corrosion: Role of various green rust compounds. *Corros. Sci.* **1997**, *39*, 1699–1710. [[CrossRef](#)]
97. Génin, J.M.R.; Refait, P.; Olowe, A.A.; Abdelmoula, M.; Fall, I.; Drissi, S.H. Identification of Green Rust Compounds in the Aqueous Corrosion Processes of Steels; the Case of Microbially Induced Corrosion and Use of 78 K CEMS. *Hyperfine Interact.* **1998**, *112*, 47–51. [[CrossRef](#)]
98. Amar, H.; Tounsi, A.; Makayssi, A.; Derja, A.; Benzakour, J.; Outzourhit, A. Corrosion inhibition of Armco iron by 2-mercaptobenzimidazole in sodium chloride 3% media. *Corros. Sci.* **2007**, *49*, 2936–2945. [[CrossRef](#)]
99. Mahdavian, M.; Ashhari, S. Corrosion inhibition performance of 2-mercaptobenzimidazole and 2-mercaptobenzoxazole compounds for protection of mild steel in hydrochloric acid solution. *Electrochim. Acta* **2010**, *55*, 1720–1724. [[CrossRef](#)]
100. Gece, G.; Bilgiç, S. Quantum chemical study of some cyclic nitrogen compounds as corrosion inhibitors of steel in NaCl media. *Corros. Sci.* **2009**, *51*, 1876–1878. [[CrossRef](#)]
101. Albrakaty, R.H.; Wazzan, N.A.; Obot, I.B. Theoretical Study of the Mechanism of Corrosion Inhibition of Carbon Steel in Acidic Solution by 2-aminobenzothiazole and 2-Mercatobenzothiazole. *Int. J. Electrochem. Sci.* **2018**, 3535–3554. [[CrossRef](#)]
102. Wang, G.; Harrison, A.; Li, X.; Whittaker, G.; Shi, J.; Wang, X.; Yang, H.; Cao, P.; Zhang, Z. Study of the adsorption of benzimidazole and 2-mercaptobenzothiazole on an iron surface by confocal micro-Raman spectroscopy. *J. Raman Spectrosc.* **2004**, *35*, 1016–1022. [[CrossRef](#)]

103. Gholami, M.; Danaee, I.; Maddahy, M.H.; RashvandAvei, M. Correlated ab Initio and Electroanalytical Study on Inhibition Behavior of 2-Mercaptobenzothiazole and Its Thiole–Thione Tautomerism Effect for the Corrosion of Steel (API 5L X52) in Sulphuric Acid Solution. *Ind. Eng. Chem. Res.* **2013**, *52*, 14875–14889. [[CrossRef](#)]
104. Wang, C.T.; Chen, S.-H.; Qi, C.-S. Protection of copper corrosion by carbazole and N-vinylcarbazole self-assembled films in NaCl solution. *J. Appl. Electrochem.* **2003**, *33*, 179–186. [[CrossRef](#)]
105. Şahin, M.; Bilgiç, S.; Yılmaz, H. The inhibition effects of some cyclic nitrogen compounds on the corrosion of the steel in NaCl mediums. *Appl. Surf. Sci.* **2002**, *195*, 1–7. [[CrossRef](#)]
106. Zhou, G.P.; Liu, Z.Y.; Qiu, Y.Q.; Wang, G.D. The improvement of weathering resistance by increasing P contents in cast strips of low carbon steels. *Mater. Des.* **2009**, *30*, 4342–4347. [[CrossRef](#)]
107. Sahoo, G.; Fujieda, S.; Shinoda, K.; Suzuki, S. Influence of phosphate species on green rust I transformation and local structure and morphology of γ -FeOOH. *Corros. Sci.* **2011**, *53*, 2446–2452. [[CrossRef](#)]
108. Sankara, T.S.N. Surface pretreatment by phosphate conversion coatings—A review. *Rev. Adv. Mater. Sci.* **2005**, *9*, 130–177.
109. Nespolo, M. Iron Metabolism. From Molecular Mechanisms to Clinical Consequences. *Acta Crystallogr. Sect. D Struct. Biol.* **2017**, *73*, 952–954. [[CrossRef](#)]
110. Skinner, H.C.W. Phosphates Geochemical, Geobiological and Materials Importance.: Edited by Matthew, J.; Kohn, John Rakovan and John, M. Hughes. Reviews in Mineralogy and Geochemistry, Vol. 48 (2002). Mineralogical Society of America, 1015 Eighteenth Street, Washington, D.C. 20036, U.S.A. US \$40, \$30 to MSA, GS, CMS members (ISBN 0 939950 60 X). *Can. Mineral.* **2003**, *41*, 1071–1073. [[CrossRef](#)]
111. Guilbaud, R.; White, M.L.; Poulton, S.W. Surface charge and growth of sulphate and carbonate green rust in aqueous media. *Geochim. Cosmochim. Acta* **2013**, *108*, 141–153. [[CrossRef](#)]
112. Huttner, G.; Strittmatter, J.; Sandhöfner, S. Phosphorus Tripodal Ligands. In *Comprehensive Coordination Chemistry II*; Elsevier Science: Amsterdam, The Netherlands, 2003; pp. 297–322. [[CrossRef](#)]
113. O’Keeffe, M. The Bond Valence Method in Crystal Chemistry. In *Modern Perspectives in Inorganic Crystal Chemistry*; Springer Science & Business Media: Berlin/Heidelberg, Germany, 1992. [[CrossRef](#)]
114. Jolivet, J.-P.; Tronc, E.; Chanéac, C. Iron oxides: From molecular clusters to solid. A nice example of chemical versatility. *C. R. Geosci.* **2006**, *338*, 488–497. [[CrossRef](#)]
115. Twigg, M.V.; Burgess, J. Iron. In *Comprehensive Coordination Chemistry II*; Elsevier Science: Amsterdam, The Netherlands, 2003; pp. 403–553. [[CrossRef](#)]
116. Downing, J.H.; Smith, M.B. Phosphorus Ligands. In *Comprehensive Coordination Chemistry II*; Elsevier Science: Amsterdam, The Netherlands, 2003; pp. 253–296. [[CrossRef](#)]
117. Das, S.; Hendry, M.J.; Essilfie-Dughan, J. Transformation of two-line ferrihydrite to goethite and hematite as a function of pH and temperature. *Environ. Sci. Technol.* **2011**, *45*, 268–275. [[CrossRef](#)]
118. Chitrakar, R.; Tezuka, S.; Sonoda, A.; Sakane, K.; Ooi, K.; Hirotsu, T. Phosphate adsorption on synthetic goethite and akaganeite. *J. Colloid Interface Sci.* **2006**, *298*, 602–608. [[CrossRef](#)]
119. Flynn, C.M. Hydrolysis of inorganic iron (III) salts. *Chem. Rev.* **1984**, *84*, 31–41. [[CrossRef](#)]
120. Navarro, J.M.; Botella, M.A.; Cerdá, A.; Martínez, V. Phosphorus uptake and translocation in salt-stressed melon plants. *J. Plant Physiol.* **2001**, *158*, 375–381. [[CrossRef](#)]
121. Hongshao, Z.; Stanforth, R. Competitive adsorption of phosphate and arsenate on goethite. *Environ. Sci. Technol.* **2001**, *35*, 4753–4757. [[CrossRef](#)] [[PubMed](#)]
122. Ler, A.; Stanforth, R. Evidence for surface precipitation of phosphate on goethite. *Environ. Sci. Technol.* **2003**, *37*, 2694–2700. [[CrossRef](#)] [[PubMed](#)]
123. Génin, J.-M.R.; Bourrié, G.; Trolard, F.; Abdelmoula, M.; Jaffrezic, A.; Refait, P.; Maitre, V.; Humbert, B.; Herbillon, A. Thermodynamic Equilibria in Aqueous Suspensions of Synthetic and Natural Fe(II)–Fe(III) Green Rusts: Occurrences of the Mineral in Hydromorphic Soils. *Environ. Sci. Technol.* **1998**, *32*, 1058–1068. [[CrossRef](#)]
124. Teodorovich, V.I.; Beznosikov, B.O. Morphological and functional study of the thrombocytes in essential polycythemia and thrombocytopenia (Werlhof’s disease). *Lab. Anal. Clin. Bacteriol. Immunol. Parasitol. Hematol. Anat. Patol. Quim. Clin.* **1961**, *39*, 77–83. [[CrossRef](#)]
125. Nriagu, J.O. Stability of vivianite and ion-pair formation in the system $\text{Fe}_3(\text{PO}_4)_2\text{-H}_3\text{PO}_4\text{-H}_3\text{PO}_4\text{-H}_2\text{O}$. *Geochim. Cosmochim. Acta* **1972**, *36*, 459–470. [[CrossRef](#)]

126. Mishra, M.; Chun, D.-M. α -Fe₂O₃ as a photocatalytic material: A review. *Appl. Catal. A Gen.* **2015**, *498*, 126–141. [[CrossRef](#)]
127. McCafferty, E. Acid-Base Properties of Surface Oxide Films. In *Surface Chemistry of Aqueous Corrosion Processes*; Springer: Berlin/Heidelberg, Germany, 2015; pp. 1–54. [[CrossRef](#)]



© 2019 by the authors. Licensee MDPI, Basel, Switzerland. This article is an open access article distributed under the terms and conditions of the Creative Commons Attribution (CC BY) license (<http://creativecommons.org/licenses/by/4.0/>).